PHYSICAL REVIEW B **109**, 104105 (2024)

Stretching-controlled structural evolution in phosphorene: Transferable and tunable twinning nanoarchitecture for construction of monatomic chains

Kun Liang and Hong Sun [*]
School of Physics and Astronomy and Key Laboratory of Artificial Structures and Quantum Control (Ministry of Education), Shanghai Jiao Tong University, Shanghai 200240, China

(Received 18 December 2023; revised 4 February 2024; accepted 12 February 2024; published 6 March 2024)

As the ultimate one-dimensional (1D) systems, ordered assemblies of monatomic chains, bound stably on the surface of thin atomic layers with good transferability, attachability, and twistability, can be used to construct innovative quantum structures from the ground up. Although atomic chains have been realized on high-index vicinal crystalline planes, metal surfaces, etc., their easy exfoliation, displacement, and shape manipulation remain difficult due to the rigidity of the solid templates. Phosphorene has intriguing physical and electronic properties, most notably in its tunable strain engineering capability and anisotropic structures. Previous studies, especially the structural response under stresses, have predominately been limited to 0 K, with phosphorene's accurate behaviors at room temperature yet to be comprehensively explored. Here, we report a computational study based on density functional theory at 300 K, which uncovers a twinning-mediated structural transformation in phosphorene in response to in-plane strains, in contrast to the conventional understanding of its intrinsic properties. Interestingly, the discovered 1D twinning channel with strong capabilities to capture and localize free atoms demonstrates its potential as an outstanding template in the construction of diverse self-assembled, long-range-ordered monatomic chains. Most importantly, aided by the inherent flexibility of phosphorene film, the monatomic chains can be easily transferred and attached to couple with other systems, or manipulated into a variety of curvilinear formations that possess unique spin configurations. This work is potentially extendable to other phosphorene analogs, enriching the toolbox for the development of transferable, attachable, and twistable atomic nanoarchitectures and paving the way to new paths for the fundamental study of low-dimensional systems.

DOI: 10.1103/PhysRevB.109.104105

I. INTRODUCTION

Atomic chains or wires represent the one-dimensional (1D) system at the ultimate scale, displaying unique topological configurations and significantly enhanced quantum effects. The ballistic motions of electrons result in quantized electronic and thermal conductance [1–5], where the current density can reach up to 10^{10} A/cm^2 [6], and additionally, single-atom switches or gaps have been realized based on stretching operations of atomic chains [7]. Besides, 1D quantum plasmons reported in metallic atomic chains can strongly couple with lights, due to the large electric dipoles of electrons in collective excitation states [8–13]. The easily tunable plasmon states facilitate devices at the atomic scale to integrate photons and electrons together with applications in signal transmission and quantum antenna design [14–16]. Furthermore, the competition between electron-electron and electron-phonon interactions, as well as electron couplings between atomic chains and their substrates, leads to diverse quantum phases like Tomonaga-Luttinger liquids (TLLs), charge density waves (CDWs), Mott insulators, etc. [17–19]. In particular, the TLL phases in atomic wires manifest unique power-law relationships in the density of states (DOS) for their low-energy collective excitations. Accompanying this is the intriguing phenomenon of spin-charge separation, which is observable under certain ranges of power-law exponents in their one-particle spectral functions [20–22]. Besides, the topological solitons, which are atomic-size in-gap defects joining degenerate CDW ground states, are demonstrated in atomic wire CDW phases with proposed algebraic operation functionalities in quantum computations [23–25].

A special class of chains with local magnetic moments are characterized as atomic spin chains (ASCs), which exhibit an impressive spectrum of excitation modes and magnetic behaviors when coupled with various substrates [26]. Particularly, ASCs made of transition metal atoms on substrates can highly maintain the 1D characteristics due to their localized d-orbital electrons. Such ASCs comprise diverse magnetic spin configurations, yielding a plethora of quantum functionalities suitable for optimized spin state choices and further utilization in quantum computing. For instance, ferromagnetic atomic chains in proximity to conventional superconductors with pronounced spin-orbit couplings lead to the emergence of Majorana zero modes (MZMs) on both ends of the chain. The MZMs are widely searched as possible candidates for constructing fault-tolerant topological qubits owing to their non-Abelian braiding statistics feature [27–29]. Moreover, antiferromagnetic ASCs that are connected to two spin input ports and joined on their other ends by an extra atom

---

[*] hsun@sjtu.edu.cn

can form a magnetically frustrated triplet gate. Such setups have been realized for executing a variety of all-spin-based logic gate operations [30]. Additionally, ASCs with helical spin configuration have been predicted to induce strong spin-orbit interactions and equivalent magnetic fields, which support topological superconductivity and Majorana fermions when placed near s-wave superconductors [31]. Moreover, the chiral spin states can be induced by the Dzyaloshinskii-Moriya (DM) or Ruderman-Kittel-Kasuya-Yosida (RKKY) interactions between the atomic chains and the substrates, thus enabling the transportation of magnetic information from externally connected magnetic islands to other ends of ASCs [32,33].

Atomic chains are at the forefront of nanoscale research, yet the free-standing chains suffer from inherent instability. Hence, their practical realization necessitates integration or coupling with supportive substrates to ensure stability. Furthermore, the recent developments in low-dimensional physics, such as spin-ring molecular qubit designs and curvilinear nanomagnetism (see discussions below), underscore the pressing need to construct atomic chains stably localized on atomic-thin layers that are easily transferable, attachable, and twistable. Unfortunately, this remains unattainable using the currently predominant experimental strategies. For example, the use of a scanning tunneling microscope (STM) allows for atomically precise operation, but is time consuming and inefficient [34,35]. The epitaxial deposition of atoms on high-index vicinal crystalline stepped surfaces, while more efficient in creating atomic arrays, is difficult to be transferred, displaced, and twisted due to their solid substrates [36,37]. Moreover, employing nanotubes to encapsulate atoms can highly align their positions, while disadvantages arise from the fact that the envelopment of the atomic chains by the nanotubes can subsequently shield their interactions with other parts needed to construct various devices [38–40]. In light of these challenges, researchers are dedicated to searching for a template that can confine atoms in one dimension with easy detection and interaction functionality while being flexible enough to allow for its straightforward transformation and shape manipulation.

Scrutinizing various potential structures, we position phosphorene as an optimal candidate for a template material to meet such demands due to its puckered structure, robust adsorption capability, and our discovered 1D twinning grain boundary emerged under tensile deformations at room temperature. As a p-type semiconductor, phosphorene features a layer-dependent direct band gap ranging from 0.3 to 2.0 eV [41,42], which lies in between those of the commonly studied two-dimensional (2D) materials like graphene (0 eV) [43] and transition metal dichalcogenides (TMDs, 1.5–2.5 eV) [44,45]. Such a tunable band gap widely spans the spectrum from mid-infrared to visible light, underlining its potential as a versatile material for optoelectronic applications. Besides, phosphorene's anisotropy in electronic and thermal transport properties is particularly pronounced. Charge carrier mobility in phosphorene varies starkly between the zigzag (with electron and hole mobility of 80 and 10 000–26 000 $\text{cm}^2\ \text{V}^{-1}\ \text{s}^{-1}$, respectively) and armchair (1100 and 640–700 $\text{cm}^2\ \text{V}^{-1}\ \text{s}^{-1}$) orientations [46]. Similarly, the thermal conductivities along these orientations differ substantially, measured as 36 $\text{W}\ \text{m}^{-1}\ \text{K}^{-1}$ along the zigzag direction and 110 $\text{W}\ \text{m}^{-1}\ \text{K}^{-1}$ along the armchair direction at 300 K [47]. Most importantly, owing to the intriguing puckered structure, phosphorene exhibits remarkable flexibility and elasticity, which can withstand a large strain of around 30%, and may undergo a ferroelastic phase transition during the stretching deformation process [48]. Such mechanical properties enable easy manipulation of its optical, electrical, and thermal properties and geometrical shape through strain engineering methodologies [49–51], making phosphorene a promising next-generation curvilinear nanoelectronic and nanomagnetic material. Despite these exceptional properties, it is unfortunate that the major theoretical calculations on phosphorene's anisotropy and mechanical behaviors, especially its structural response under stresses, are restricted to 0 K. Researches that accurately elucidate these properties at room temperature are notably sparse—yet vital for practical use. In fact, our investigation on phosphorene discovers a deviation from the expected behaviors extrapolated from previous theoretical studies carried out at 0 K. At 300 K, uniaxial stretching along the zigzag direction leads to the emergence of an independent 1D twinning structure. Surprisingly, this structure retains all the advantageous characteristics that are ideal for the creation of one-dimensional atomic chain templates, as described above.

The integration of flexible phosphorene films with atomic chains shows significant potential in its capacity to engender intricate curvilinear nanoarchitectures at the atomic scale. Recently, the relevant research on curvilinear systems has extensively attracted keen interest, since the twisted and bent magnetic wires and films with multifarious curvature and torsion exhibit more captivating geometry-induced effects, which have a profound impact on the magnetic behaviors through induced anisotropy and DM interaction. For example, the curved nanowires composed of permalloy ($\text{Ni}_{81}\text{Fe}_{19}$) stand out for their domain-wall dynamics, offering groundbreaking designs for high-performance and low-power spintronics-based memory device applications, which may reach a storage density of 100 times higher than the current capabilities [52,53]. These domain walls exhibit manipulable behaviors via spin-polarized currents, imbuing them with the prospects of acting as high-speed storage units due to their rapid response times and high velocities [54]. Besides, chiral effects have been experimentally observed in the parabolic-shaped permalloy, which can be fine tuned by the curvature and width. By measuring the depinning field in the parabolic stripes where domain walls are expelled, the DM interactions are quantitatively assessed, providing insights into the relationship between material curvature and chiral magnetic behavior [55]. Likewise, the utilization of direct-write nanofabrication techniques has led to the creation of intertwined nanomagnetic cobalt (Co) double helices [56,57]. These helical configurations demonstrate stable magnetic states emergent from strong coupling at their junctions, and showcase the interplay of curvature, torsion, and chirality effects. Similar helical structures can even find application in the field of remotely controlled robotic microswimmers, since their chiral architecture can be driven by the external rotating homogeneous magnetic field [58]. Additionally, the rolled-up sensors based on giant magnetoresistance (GMR) or giant magnetoimpedance (GMI) effects demonstrate drastically improved magnetoelectrical performance. It has been reported that such three-dimensional (3D) architecture can provide an increase in sensitivity of 80 times, capable of detecting subtle magnetic fields with responses starting as low as 45 μV Oe^{-1}, and the unique design of these sensors suggests utilization in omnidirectional signal detection. Hence, they are perfectly poised for embedding into flexible, shape-conforming electronics such as in-body sensors or electronic skin (e-skin) [59–61].

Atomic rings are a special class of curvilinear structures, with the simplest nonlinear topological configuration, but possessing nearly inexhaustible application potentials. Research in this area frequently focuses on magnetic molecular wheels, divided into ferromagnetic and antiferromagnetic categories. For example, ferromagnetic atomic spin rings (ASRs) like Mn_{12} display quantum magnetization tunneling under magnetic fields [62–64], and their applications in quantum computing with an implementation of Grover's algorithm were proposed, where spin anisotropy plays a crucial role in both cases [65]. The large total spins in the ground states of the ferromagnetic ASRs make them behave like single-molecule magnets with nanometer sizes. Applications in molecular spintronics, encompassing the design of molecular spin transistors, molecular spin valves, etc., are demonstrated [66,67]. In comparison, the antiferromagnetic ASRs are naturally more resistant to external magnetic fields [68]. In Fe_{10} and Cr_8 ASRs [69,70], level crossings (LCs) from the ground to low-lying energy states due to the Zeeman effect are observed in the presence of an external magnetic field at low temperature [69]. These LCs enhance quantized step magnetization and imply intriguing behaviors and applications. Examples include spin Peierls instability, like that in $CsFe_8$ [71], where DM interactions may occasion bond distortions, thereby transforming the system into dimerized spin rings [72]—a novel prospect for investigating Bose-Einstein condensation (BEC) of bosonic magnetic triplons [73–75]. Besides, the induced LCs also affect the spin properties of the ASR's ground states and relevant temperature–magnetic field (T-B) relations in isentropes, which can be leveraged in cryogenic cooling to sub-Kelvin level by means of antiferromagnetic $Gd_{12}Na_6$ double rings [76] or frustrated Gd_7 rings [77]. Furthermore, heterometallic ASRs, exemplified by Cr_7M (where M can be Ni, Mn), have been synthesized with spin degenerate ground states of total spin $S = 1/2$ or $S = 1$. These can be fine tuned with a magnetic field into effective two- or three-level systems while maintaining energy gap separation from higher excited states, suggesting an attribute conducive to qubit design [78]. Remarkably, these systems can maintain a phase-decoherence time of up to 15 μs, which surpasses the quantum manipulation timescales ($\sim$10 ns) [79]. The molecules' relatively larger size eases the magnetic field spatial resolution requirements and promotes precise isolation of individual qubits [78]. Furthermore, such magnets can be connected into robust quantum arrays, holding promising prospects for the realization of reliable quantum gates and quantum information storage designs [79–81].

In this work, employing first-principles molecular dynamics calculations, we discover twinning structures in phosphorene induced by in-plane stretching at room temperature. The twinned phosphorene reveals an entirely different stress response mechanism characterized by continuous structural transformations induced by the symmetric twinning grain boundaries thereof, resulting in a tunable anisotropy that diminishes continuously from pronounced to nearly imperceptible under increasing strain, marked most prominently by the change of the electron (hole) effective mass ratio in the zigzag and armchair directions from 9.4 to 1 (70.2 to 1). This renews our comprehension of phosphorene's inherent characteristics and corresponding applications, as well as of its analogs including arsenene, antimonene [82,83], etc. More importantly, we prove the twinned phosphorene is a superior template for constructing ordered and stable 1D atomic chains, with adsorption energies of $3d$ transition metals on tops of twinnings nearly 1 eV larger than those at the next nearby adsorption locations, which manifest ferromagnetic and antiferromagnetic orders, as well as the modulated CDWs. Moreover, benefiting from its puckered structure, the monolayer twinned phosphorene template shows remarkable softness and resilience. These traits allow for ease of manipulation and enable the film itself to be transferred and attached over bulk structures, or to be twisted into helical, chiral, and spiral configurations to produce more intricately coupled 1D structures. As a simple show-how, we construct an end-to-end atomic ring by curving the atomic chain, and it exhibits the Jahn-Teller-effect-dominated [84] structural distortion, forming ferro- and antiferromagnetic dimer spin rings. Notably, our constructed monatomic chains and rings are exposed on the surfaces of twinned phosphorene, making them easy to be transferred, attached, and twisted in practical applications. A thorough understanding of these phosphorene twinning structures, expected to be generated effectively by simple stretching at room temperature, will open up new prospects in the study of low-dimensional physics, stimulate innovative ideas for designing diverse monatomic devices, and bring about breakthroughs in nanoelectronic and nanomagnetic technologies.

II. METHODS

The first-principles calculations are conducted using the Vienna *Ab initio* Simulation Package (VASP) codes [85], where the electron-ion interaction is described with projector augmented wave (PAW) pseudopotentials [86], while the exchange-correlation interaction is treated via the generalized gradient approximation (GGA), as parametrized by Perdew, Burke, and Ernzerhof (PBE) [87]. In the computation, a supercell encompassing 72 atoms, as depicted in Fig. 1(a), is chosen, separated by a vacuum layer 15 Å thick to nullify the interlayer interactions. Furthermore, we designate the cutoff energy of 500 eV and the Monkhorst-Pack k-point grid as $5 \times 5 \times 1$ [88]. The convergence thresholds for total energy and the Hellmann-Feynman force on atoms are set to 1×10^{-5} eV and 0.01 eV/Å, respectively, and the van der Waals energy correction is considered using the DFT-D3 dispersion relation [89]. Also noteworthy is that for adsorption calculations, the influence of spin polarization is considered, and the migration energy barriers are calculated using the climbing image nudged elastic band (CI-NEB) methodology [90,91].

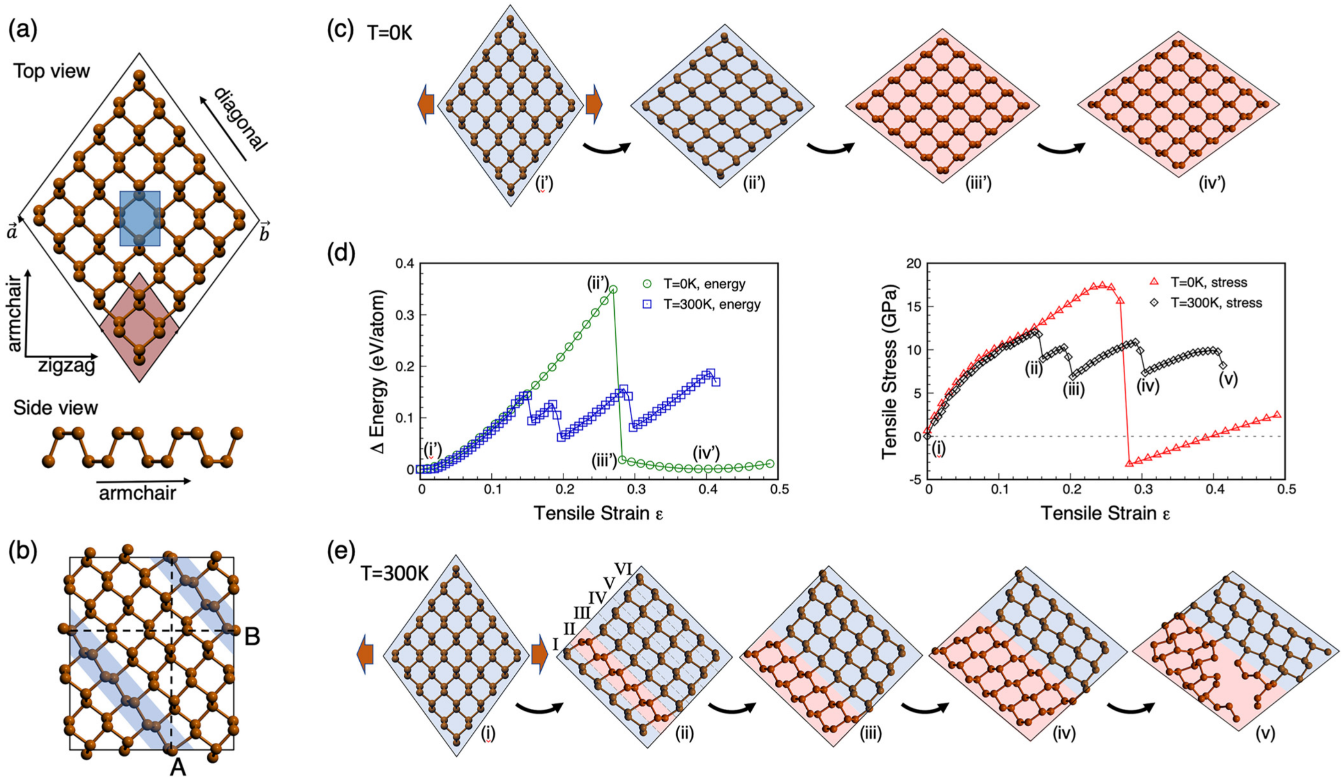

FIG. 1. (a) Top and side views of pristine phosphorene, where the red shaded area is our chosen unit cell, and the blue one is the common Wigner-Seitz cell, respectively. (b) The commonly used supercell, where the chains alternate the orientations in pairs under tensile strains along the zigzag direction due to the boundary conditions, marked by the dotted lines. (c) The structural transformation process of phosphorene's ferroelastic phase transition at 0 K, when subjected to tension along the zigzag direction. The domains retaining their orientations versus those altering orientations are highlighted in blue and red shading, respectively. (d) Calculated energy-strain (left) and stress-strain (right) relationships of phosphorene at 0 K and room temperature (300 K), with the strain applied in the zigzag direction. (e) The structural transformation due to the twinning-induced transition mechanism under the 300 K tensile process. In subplot (ii), atoms are partitioned into six distinct chains, sequentially numbered from I to VI.

The application of the well-developed quasistatic continuous stretching calculation method is detailed next [92,93]. For the case at zero temperature (0 K), tensile strain is applied incrementally in a chosen direction with a strain increase $\Delta\varepsilon = 0.01$ at each step, and then the component of the stress tensor along the stretching direction is fixed, while the other tensor components, along with all atoms, are allowed to fully relax before stretching to the next step. Similarly, the 300 K temperature stretching calculation mirrors the one adopted at 0 K, starting from the equilibrium structure averaged at the given temperature. After incrementally applying the strain to the thermally averaged structure obtained in the previous step, a modified Parrinello-Rahman (*NpT*) *ab initio* molecular dynamics (AIMD) relaxation of 3000 steps is implemented [94], where we change the VASP AIMD code to constrain the relaxation so that the strain in the stretching direction does not change within the *NpT* ensemble at finite temperature [95,96]. During the AIMD simulation within each increment of strain, specified by $\Delta\varepsilon = 0.01$, only the five independent components of the strain tensor in directions different from that of stretching and all the atoms in the supercell undergo simultaneous AIMD relaxation. Each relaxation phase comprises 3000 steps under given constraints, where the stipulated convergence criteria for each step are (i) the absolute value of all five stress tensor components in directions different from stretching are less than 0.1 GPa, and (ii) the applied average force on each atom is kept within 0.01 eV/Å. Herein, the initial 1000 steps, possibly showing large fluctuations, are disregarded, whereas the subsequent 2000 steps are statistically analyzed to derive the physical quantities, including the thermal average structure for the next stretching step. The lowered convergence criteria for the finite-temperature computation allow for a marginal reduction in the cutoff energy and vacuum layer thickness—setting them to 450 eV and 12 Å, respectively—in order to expedite the management of the voluminous data. The time step of the AIMD simulation is set as 2 fs, while the constant temperature during the simulation is controlled by the Langevin thermostat [97].

III. RESULTS AND DISCUSSION

A. The twinning-induced transition mechanism

The stress response mechanism of phosphorene has inspired an extensive range of research themes such as mechanical strength [98], band-gap modulation [99], and anisotropic transportation characteristics [49,100]. These previous studies have identified a ferroelastic transition mechanism in phosphorene, associated with a 90° orientation alteration under stretching along the zigzag direction [101,102]. However, in our study, we discover an intermediate state with twinning structures in phosphorene stretched at room temperature, preceding much earlier that of the ferroelastic transition during stretching. The conventional supercell selections, represented by the blue shaded area in Fig. 1(a), introduce artificial effects in the analysis of the twinning mechanism. For the purpose of illustration, Fig 1(b) demonstrates that stretching the rectangular supercell along the zigzag direction leads some chains to switch their orientations to form twins. The issue is that chains A and B [highlighted within the blue-hued region in Fig. 1(b)] are correlated by the artificial periodic boundary conditions of the supercell, indicated with dashed lines, thereby undergoing simultaneous transitions in their orientations. In fact, the chains enclosed within the supercell should be unrelated, and special care should be taken to avoid artificial correlations of the boundary atoms in the structural phase transition process. A recent study on the tensile process of phosphorene at room temperature particularly shows such effects arising from the particular selection of unit cell [103]. To rectify this, we introduce a unit cell orienting diagonally across phosphorene, represented by the red shading in Fig. 1(a). This ensures that each atom (or atomic chain) falls within the supercell border, and can be individually dealt with, unconfined by boundary conditions. Subsequent calculations employ an expanded 3 × 3 × 1 supercell, viewed from the top and side perspectives as showcased in Fig. 1(a).

Using this configuration, we simulate phosphorene structure evolution under tensile conditions at both 0 and 300 K (room temperature), and the transformations are displayed in Figs. 1(c) and 1(e). The blue and red shaded areas independently represent domains preceding and succeeding the orientation shift of atomic bonds. The energy-strain and stress-strain relationships for stretching at 0 and 300 K are also demonstrated in the left and right graphs of Fig. 1(d). In Fig. 1(c), the known phenomenon of ferroelastic phase transition in phosphorene is reproduced. As the structure evolves from the primary tensile position (i′) to a final structure (iv′), it experiences a sudden 90° orientation transition of the whole lattice structure. The intermediate structures, (ii′ and iii′) correspond closely to a 27% strain, and are the critical structures before and after the transition. The green line in Fig. 1(d) corresponds to the ferroelastic transition process, with the four corresponding stages (i′–iv′) marked inside. This process is a global structural transformation where all atomic bonds reform simultaneously, so it demands overcoming a relatively high energy barrier, leading to a deep drop in total energy and stress associated with the abrupt orientation change of ferroelasticity.

In contrast, the process of stretching phosphorene at room temperature [Fig. 1(e)] demonstrates wholly different stress response characteristics. Starting from the thermal equilibrium structure, the orientation transition of phosphorene follows a stepwise pattern from stages (i) to (v), and during each phase, only a fraction of phosphorous atoms switch their orientations. The phosphorene structure falls short of a complete 90° structural transformation, descending into disintegration once half of the atoms have transitioned. For an exhaustive explanation of the tensile process at 300 K, we employ dotted lines to subdivide the atoms in the supercell into six atomic chains, labeled as I–VI in Fig. 1(e-ii). Transitioning from stage (i) to stage (ii), only chain II experiences an orientation change, while the remaining chains stay unchanged. As the tensile strain increases, contiguous chains switch their orientations one at a time until the red shade extends to encapsulate half of the supercell, depicted in structure (iv). Consequently, the system evolves into a wholly symmetric twinning structure in Fig. 1(e-iv), with the twinning grain boundary (TGB) intersecting the red and blue domains. Continuing to augment the tension, the system is consequently unable to bear the accruing stretching force and ultimately ruptures, as illustrated in Fig. 1(e-v). Although the total energy of the lattice drops slightly when twinning forms, it continuously accumulates and increases within the system due to the deformation of atomic bonds during the tensile process, as shown by the blue curve in Fig. 1(d), which finally surpasses the structural threshold and precipitates the system's failure. The structures (i)–(v) are also correspondingly marked near the black curve in the right graph of Fig. 1(d). Since the stretching process at 300 K is a more localized and gradual structural transformation compared to that at 0 K, it is associated with lower energy barriers, resulting in smaller reductions in energy and less stress release. The exact AIMD simulation times, at which the structural transitions in Figs. 1(e-i)–1(e-v) occur throughout different 3000-step AIMD relaxations during tensile strain incremental increase steps, can be determined by examining the intermediate structural deformation states and the critical transition points through analyzing the energy variations during the AIMD relaxations. The results are presented in the Supplemental Material (see Fig. S1) [104].

From the analysis, we obtain that phosphorene could retain its superelastic properties at room temperature, enduring up to 40% strain. More critically, it introduces an entirely novel stress response mechanism in comparison with the previously established ferroelastic phase transition theories. In an effort to augment the understanding of this twinning mechanism, we supplement with two essential analyses at 0 K to yield profound insights. First, utilizing the CI-NEB method at 0 K, we unveil that the energy barrier associated with the twinning-induced process (0.05 eV/atom) is markedly lower than that of the ferroelastic transition process (0.15 eV/atom). Second, it is observed that the chains transition their orientations sequentially and adjacently, rather than in a random manner. To find the underlying reasons for this phenomenon, we calculate all of its isomers with nonadjacent twinning structures and compare the energies of different configurations. Detailed analyses on these aspects are provided in the Supplemental Material (see Figs. S2 and S3) [104].

B. The intrinsic characteristics of the twinned phosphorene

The twinning structure of phosphorene, as depicted in Fig. 1(e-iv), is symmetric about the TGB, presenting an identical structure to pristine black phosphorene on either side. Thus, the TGB can be considered a line defect within the phosphorene lattice. The stability of the TGB can be ascertained by comparing the energy associated with the twinning to those of the line defects observed in phosphorene, where we define the defect energy E_{defect} as the energy increment per unit length introduced by the line defect to the phosphorene system according to Eq. (1):

$$E_{\text{defect}} = \frac{E_{\text{system}} - nE_{\text{P}}}{Nl}, \tag{1}$$

where E_{system} is the total energy of the system, n stands for the number of atoms, E_{P} represents the average energy of a single atom in pristine phosphorene, and N and l account, respectively, for the quantity and length of the line defects. In phosphorene, various line defects have been investigated, and the corresponding energies have been reported to vary on the order of 10^{-1} eV, with typical values such as 0.308 eV/Å for H_{48}, 0.118 eV/Å for H_{57}, 0.106 eV/Å for δ, and 0 eV/Å for β line defects [105,106]. Notably, defect energies less than 0.01 eV/Å are considered extremely low and indicative of superior stability. Within our investigation, the twinning structures we examined exhibited a line defect energy of 0.06 eV/Å, lower than many of these line defects. Besides, the orientation of the TGB aligns with the diagonal direction in phosphorene, as illustrated by the arrows in Fig. 1(a). Therefore, if a fracture of the system occurs along the TGB line defect, it would produce an edge structure identical to that formed by bond breaking along phosphorene's diagonal direction. The energy of this edge structure, denoted as E_{edge}, is calculated in the same manner as the defect energy formulated in Eq. (1). We have determined that the edge energy along the diagonal direction is approximately 0.32 eV/Å. Thus the significant increase of the energy value suggests that the spontaneous breakdown of the twinned phosphorene along the TGB is unfavorable under room-temperature disturbance. Most importantly, the remarkably low value of the TGB's line defect energy suggests that the twinning structure possesses considerable inherent stability, and such structure could be generated naturally through simple stretching at room temperature, making it a promising nanoarchitecture for further decoration, manipulation, and eventual practical applications.

The twinned phosphorene introduces distinctive mechanical and electronic properties and, therefore, pioneers new understandings in its room-temperature applications. To elaborate on these emergent characteristics, we examine the structures obtained by stretching at 300 K, as shown in Figs. 1(e-i)–1(e-iv). We first allow them to undergo full relaxation at 0 K to obtain their stable supercells, and the pristine phosphorene and half-transitioned twinned phosphorene are first investigated, as respectively depicted on the right of Figs. 2(a) and 2(b). Subsequent comparisons involving their band structures and DOS are made and represented on the left portion of the figure, with the first Brillouin zones incorporated as insets in the central part. Our investigation manifests that tensile deformation reduces the band gap of the system. However, it is inspiring to see that twinned phosphorene unwaveringly retains a direct band gap, ensuring its applicability in electronics and photonics unscathed.

As for transport properties, phosphorene has already been distinguished as a compellingly anisotropic material. Preceding work posited that the ferroelastic phase transition phenomenon could trigger a drastic 90° shift in the preferential direction of transport under the influence of applied stress. However, our present investigation establishes that under the room-temperature condition, the actual transition stage is dominated by the twinning-induced mechanism, thereby implying distinctively contrasting transport characteristics under applied stress. To show this, we first conduct an analysis of the projected density of states (PDOS), and find out that for the charge carriers near the Fermi surface and the overall twinned phosphorene, their orbital occupancy characteristics remain almost unchanged. More detailed results and discussions can be found in the Supplemental Material (see Fig. S4) [104]. Considering the altered symmetry in twinned phosphorene, we propose a quantitative assessment of transport properties by evaluating effective masses along different orientations in reciprocal space (K space), which are inversely proportional to the conductivities of the charge carriers.

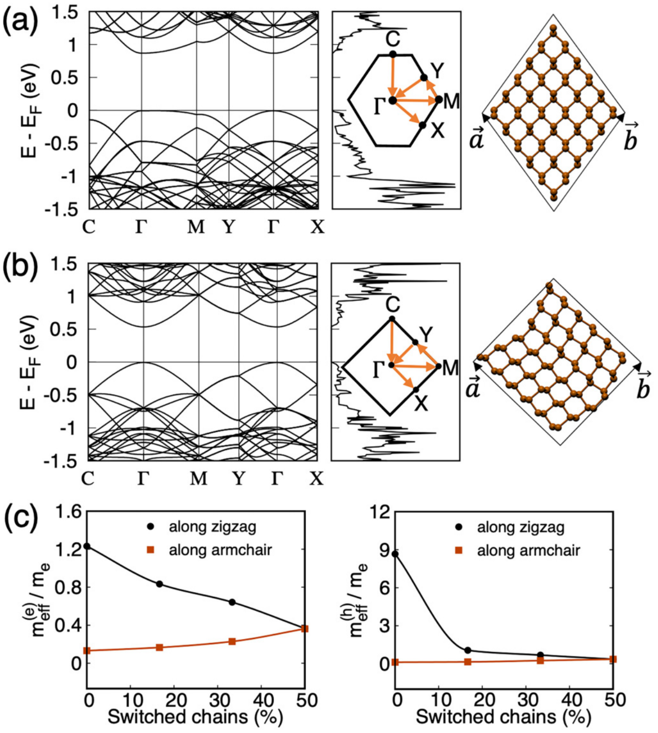

FIG. 2. The impact of twinning on the electronic properties of phosphorene, wherein the twinned phosphorene structures are obtained by stretching phosphorene at 300 K, as shown in Figs. 1(e-i)–1(e-iv), and then fully relaxed at 0 K. [(a) and (b)] Band structures and density of states (DOS) of pristine phosphorene and the half-transitioned twinned phosphorene, whose atomic structures are represented on the right. The accompanying insets in the middle illustrate their respective first Brillouin zones and k paths. (c) The calculated effective masses of electrons (left) and holes (right) along the zigzag (black) and the armchair (red) directions, where the structures with different switched chain ratios correspond to the ones in Figs. 1(e-i)–1(e-iv) that are fully relaxed at 0 K.

The effective mass is derived from the second-order derivative ($m_{\text{eff}} = \pm\hbar^2(\frac{d^2E_k}{dk^2})^{-1}$) along the path within the first Brillouin zone according to the band structure. As the tensile strain incrementally escalates, atomic chains successively alter their orientations until the ratio of switched chains attains 50%, and the alternation in the effective mass of the electron and the hole is demonstrated separately in the left and right graphs in Fig. 2(c). Considering two specific directions, namely, the zigzag and the armchair orientations, we discern that the effective mass of the carriers (accounting

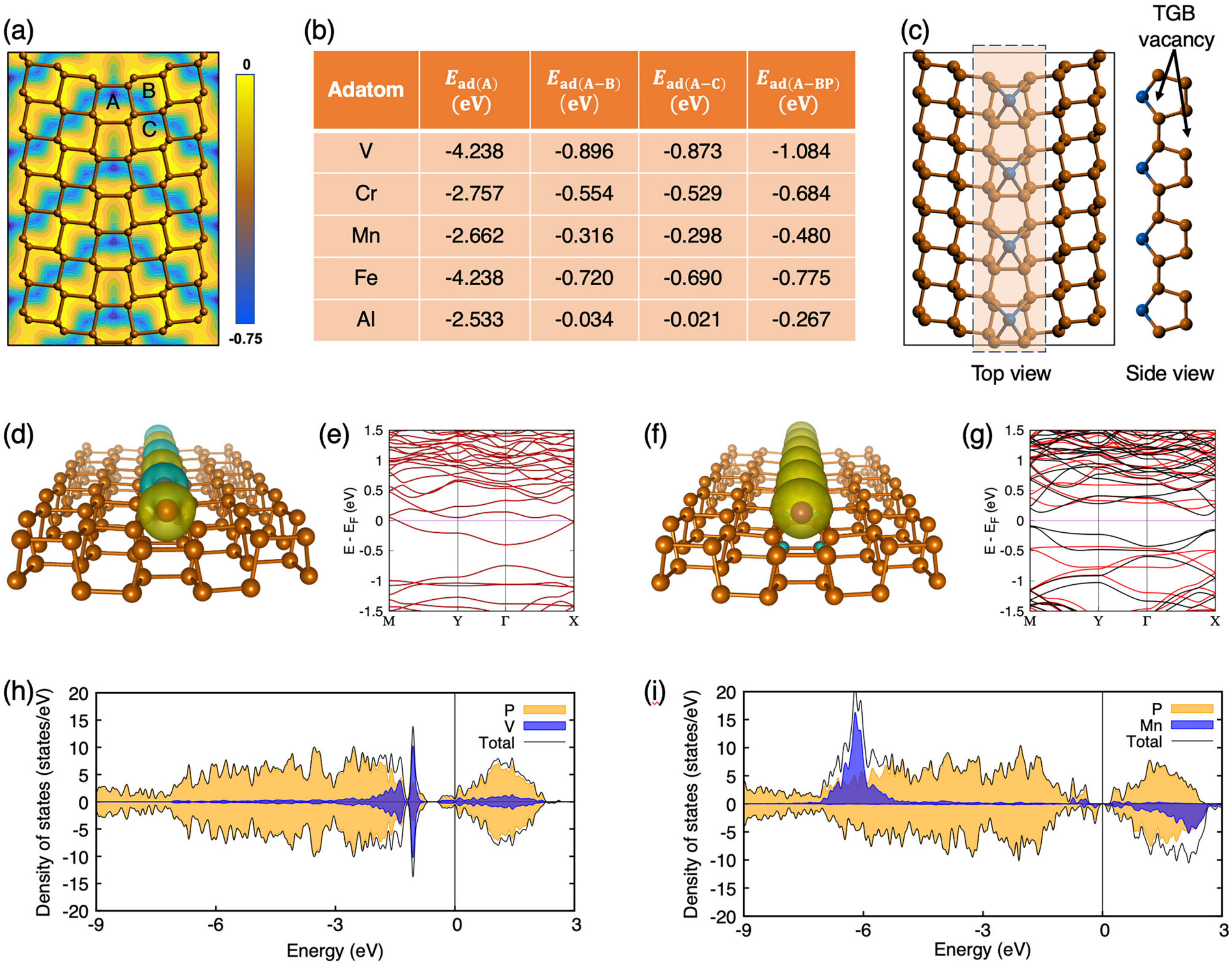

Adatom	$E_{\mathrm{ad(A)}}$ (eV)	$E_{\mathrm{ad(A-B)}}$ (eV)	$E_{\mathrm{ad(A-C)}}$ (eV)	$E_{\mathrm{ad(A-BP)}}$ (eV)
V	-4.238	-0.896	-0.873	-1.084
Cr	-2.757	-0.554	-0.529	-0.684
Mn	-2.662	-0.316	-0.298	-0.480
Fe	-4.238	-0.720	-0.690	-0.775
Al	-2.533	-0.034	-0.021	-0.267

FIG. 3. (a) The supercell used to calculate maps of the spatial distribution of the differential total energy [$E_{\mathrm{diff}} = E_{\mathrm{total}} - \max(E_{\mathrm{total}})$] for Mn within various sites of the twinned phosphorene, where the size of the phosphorus atoms has been reduced to prevent obstruction of a clear heat map. (b) The calculated adsorption energies of distinct atoms (including V, Cr, Mn, Fe, and Al) adsorbed on sites A, B, and C and pristine phosphorene upon complete relaxation. The energies are benchmarked against the adsorption energy at site A, which is set as the reference. (c) The top (or side) view of the supercell used to calculate atomic chains on the twinned phosphorene with the twinning grain boundary highlighted in red and the adsorbed atoms represented in blue. (d) The spin charge density difference ($\rho_{\mathrm{diff}} = \rho_{\mathrm{spin}\uparrow} - \rho_{\mathrm{spin}\downarrow}$) of the V antiferromagnetic chain, with the isosurface demarcated at $0.010e/\mathrm{bohr}^3$. [(e) and (h)] The corresponding band structure and projected DOS of the V chain. [(f), (g), and (i)] Similar analysis results for the Mn ferromagnetic atomic chain, with the isosurface in (f) also demarcated as $0.010e/\mathrm{bohr}^3$.

for both electron and hole) progressively increases along the armchair direction throughout the transition process, leading to a reduction in its conductive capacity. Concurrently, the trend inversely correlates for the case in the zigzag direction. As such, the anisotropy gradually weakens and almost disappears until the switched chains' ratio reaches 50%, when the structure becomes identical along the initial zigzag and armchair directions. Consequently, the novel characteristics of the twinned phosphorene make it possible to continuously control its anisotropy, bringing about potential applications in transport devices.

C. The atomic chains constructed using the TGB template

Existing research has unveiled that defects in phosphorene appreciably amplify its adsorption ability [107–109]. Particularly intriguing is the TGB, where we find it as a line defect that demonstrates a superior capability in capturing and localizing adatoms, making it an ideal template for constructing 1D atomic chains. To demonstrate that the TGB can effectively trap metal atoms in a line, we compare the adsorption stability of a single metal atom at each site on the twinned phosphorene.

First, we fix the template and the XY coordinate of the adsorbed atom, while allowing the adatom to freely relax only in the Z direction to deduce the total energy of the system. The atomic structure of the supercell used in the calculations is illustrated in Fig. 3(a) with periodic boundary conditions. Under this setup, we divide the supercell into a 60 × 100 grid, placing the adsorbed atom sequentially at each intersection site of the grid and determining the corresponding energy landscape of the system. A heat map is delineated that precisely profiles the variations in total energies, which equal the variations in absorption energies, across different positions on the twinned phosphorene, where the maximal absorption energy is set as the reference zero energy point, and Fig. 3(a) illustrates the result for the adsorbent Mn. Notably, the dark blue region in Fig. 3(a) signifies a higher trapping effect on the adatom, with a color scale showing that the most stable site of the Mn atom is characterized by an adsorption energy 0.75 eV lower than the maximum. It is evident from the diagram that these sites are arrayed on the vacancies along the TGB. This observation substantiates the claim that a 1D atomic chain can spontaneously form on the twinned phosphorene template. Furthermore, we considered the adsorption of several other elements: V, Cr, Fe, and Al. These corresponding adsorption heat maps are presented in the Supplemental Material (see Fig. S5) [104]. Across all instances, the results confirm the feasibility of constructing various 1D atomic chains along TGB channels.

Recognizing the significant potential of the TGB in facilitating the construction of 1D atomic chains, we then undertake a more nuanced computational analysis to ascertain the specific adsorption energies of adatoms on several locally stable sites near the TGB channel, under conditions of full relaxation. This comparative examination illuminates not only the superior capacity of the TGB to capture individual atoms, as compared to pristine black phosphorene, but also affirms the high degree of localization and stabilization of atomic chains constrained along the TGB. The concept of adsorption energy (E_{ad}) is defined herein by Eq. (2):

$$E_{\text{ad}} = \frac{E_{\text{P+X}} - E_{\text{P}} - n \cdot \mu_{\text{X}}}{n}, \tag{2}$$

where $E_{\text{P+X}}$ symbolizes the total energy of the system incorporating the phosphorene substrate and the adsorbed atoms X. E_{P} denotes the energy related to the substrate, while μ_{X} signifies the energy of a single, isolated adatom enclosed within a cubic box of side length 20 Å. Last, n quantifies the number of adatoms present in the system.

We extend our study to evaluate the adsorption energies of five diverse elements: V, Cr, Mn, Fe, and Al. Here we use the same supercell in Fig. 3(a) while letting the substrate and adatoms be fully relaxed, and the quantitative results of these explorations are presented in the table illustrated in Fig. 3(b). In this table's second column, we compute the adsorption energies of the adatoms within the TGB channel, specified as site A in Fig. 3(a). These adsorption energies are remarkably high ($|E_{\text{ad}}| > 2.5$ eV), authenticating that the insides of the TGB channels are suitable for stable adatom trapping. In appraising the superior localization ability of the TGB, we compare its adsorption energy to those of atoms adsorbed on the locally stable sites near the TGB channels [designated as sites A, B, and C in Fig. 3(a)] and on the pristine phosphorene. Corresponding energy differences are tabulated in the third, fourth, and fifth columns of Fig. 3(b). For transition metal atoms (V, Cr, Mn, and Fe), as displayed in the first four rows of the table, the disparities among these adsorption energy values are in the order of eV, indicating the predilection of these atoms to be adsorbed inside the TGB, rather than the nearby locally stable sites, let alone the regions remote from the TGB region. Conversely, the adsorption energies of Al are rather gradual across all sites, exhibiting a mere difference of tens of meV. Consequently, in the presence of thermal disturbances at room temperature, transition metal adatoms are expected to remain localized within the TGB, while Al adatoms may potentially navigate perpendicularly outside of the TGB channel. It is worth mentioning that we have conducted tests to determine whether the cell size, specifically the width, influences the adsorption energy of atoms on twinned phosphorene. We find that in our system, the width of the supercell is sufficient, and the effect of a (doubly) wider cell on the adsorption energy of atoms on twinned phosphorene could be neglected. Corresponding structures and data are provided in the Supplemental Material (see Fig. S6) [104].

In light of the compelling evidence that the twinning channel can robustly capture isolated metal atoms and ensure their high localization, twinned phosphorene is regarded as an experimental template for the self-assembly of 1D atomic chains. An illustration of this coupled system is depicted in Fig. 3(c), which is the supercell used in the calculations with periodic boundary conditions where the phosphorous substrate atoms are represented in red, while the adsorbed metal atoms are shown in blue. The TGB is spotlighted by red shading in the top view, and its corresponding side view is illustrated on the right-hand side, which also indicates that alternating vacancies are distributed on both sides of the TGB, as pointed out using the arrows. In a theoretical assumption, atomic chains could indeed be formed on either or both sides of the twinned phosphorene film. However, with a mindful eye towards experimental feasibility and utility, we elect to focus our attention primarily on the unilateral adsorption model.

In our exploration of 1D atomic chains, we initially focus on those constituted by $3d$ transition metal (TM) atoms, specifically V, Cr, Mn, and Fe. The unpaired electrons from the d orbital of the TM atom contribute to the net spin of the system, and the diverse linear arrangement of the TM atoms within the TGB may engender different stable and easy operational magnetic orders. We investigate these atomic chains within the supercell shown in Fig. 3(c), which accommodates four adatoms. These adatoms may arrange themselves into either ferromagnetic (spin ↑↑↑↑) or antiferromagnetic (spin ↑↓↑↓) configurations. Although only a pair of adatoms would suffice to illustrate these two magnetic states, we opt for a larger supercell housing four adatoms to preclude the possibility of periodic aggregation of atoms within the chains, such as dimerization or Peierls deformation. To account for the strong correlations among the d-orbital electrons of TM atoms, we exploit the GGA + U methods to enhance the precision of our results. The Hubbard U value, which may vary across different elements and systems, is determined using the linear response method [110], as described in Eq. (3):

$$U = \left(\frac{\partial \alpha_{\text{I}}^{\text{KS}}}{\partial q_{\text{I}}}\right)^{-1} - \left(\frac{\partial \alpha_{\text{I}}}{\partial q_{\text{I}}}\right)^{-1} \tag{3}$$

In this equation, $\alpha_{\text{I}}^{\text{KS}}$ and α_{I} denote the imposed Hubbard U potential shifts on site I for self-consistent and non-self-consistent calculations, respectively, while q_{I} represents the d-orbital electron occupation number of the atom at site I. By applying this method, we ultimately ascertain the U values for each type of adatom adsorbed on the twinned phosphorene

TABLE I. The comparison of energy (meV/atom) between ferromagnetic (↑↑↑↑) and antiferromagnetic (↑↓↑↓) configurations for V, Cr, Mn, and Fe, with Hubbard U values scanning from 2.0 to 6.0 eV.

U (eV)	ΔE^{a} (V)	ΔE (Cr)	ΔE (Mn)	ΔE (Fe)
2.00	14.41	29.67	−55.62	14.09
2.50	22.46	30.80	−61.33	9.04
3.00	29.40	27.11	−61.43	−1.27
3.50	34.02	23.52	−58.64	−9.00
4.00	34.53	20.44	−54.23	−13.36
4.50	32.15	17.60	−49.39	−15.95
5.00	28.95	15.38	−44.12	−17.38
5.50	25.66	13.22	−39.16	−17.96
6.00	22.24	11.15	−34.54	−18.29
Exclusive U^{b}	34.64	19.59	−45.88	−13.12

[a] $\Delta E = E_{\text{ferro}} - E_{\text{antiferro}}$ (meV/atom).

[b] The Hubbard U value is derived from the linear response method, and the exclusive values are 3.67, 4.15, 4.83, and 3.96 eV for V, Cr, Mn, and Fe, respectively.

substrate: $U = 3.67$ eV for V, 4.15 eV for Cr, 4.83 eV for Mn, and 3.96 eV for Fe.

We then determine the preferential magnetic configuration of the several atomic chains by comparing the energies of their ferromagnetic and antiferromagnetic states ($\Delta E = E_{\text{ferro}} - E_{\text{antiferro}}$) under GGA + U calculations. Considering that the selection of the U value for an element can vary across different studies, we compute the energy difference with U values scanning from 2 to 6 eV, aiming to ensure that our results remain unaffected by the choice of U values. The quantitative data are presented in Table I, where ΔE values have been averaged over each TM atom. In the final row, we calculate the exclusive result for each element using the U values derived from the linear response method. Our findings manifest that the energy of the antiferromagnetic state of the V adsorbed system is 34.64 meV/atom lower than that of the ferromagnetic state, and the ΔE value exceeds that (∼26 meV) caused by the thermal disturbance at 300 K, suggesting it to be a stable atomic chain at room temperature. Moreover, regardless of the U-value variance, the V atomic chain consistently maintains an antiferromagnetic state with lower energy, underscoring the rationality and robustness of our results. Similarly, the Mn atomic chain exhibits a stable antiferromagnetic state at any U value, with ΔE even reaching 45.88 meV/atom at its exclusive U value. Conversely, ΔE values are relatively small for the Cr atomic chain, and the Fe atomic chain does not even exhibit a preferential magnetic state. As such, these two chains do not demonstrate specific magnetic stability; thereby, our subsequent study will focus solely on the V and Mn chains.

As no relative motions of TM atoms with each other (or dimerization) are found in the above calculations, we reduce the size of the supercell in Fig. 3(c) by half along the twinning direction in the investigation of the electronic characteristics of the two types of atomic chains, aiming to present a clear band structure with minimal band folding. We first commence by plotting the spin density difference ($\rho_{\text{diff}} = \rho_{\text{spin}\uparrow} - \rho_{\text{spin}\downarrow}$) of the V antiferromagnetic chain, as illustrated in Fig. 3(d), with the isosurface cutoff value set to be $0.010e/\text{bohr}^3$. We observe that the V atoms are equidistantly arranged in a line, with the net spin-polarized charge being highly localized around them. Figure 3(e) presents the band structure of the system, where the k path is in accordance with the Brillouin zone illustrated in Fig. 2(b). The red and black lines separately represent the spin-up and spin-down components, and they perfectly overlap with each other. The bands intersect the Fermi energy, thereby classifying the system as metallic. The projected DOS, as shown in Fig. 3(h), depicts that the contribution from the TM atoms is concentrated approximately 1.5 eV below the Fermi level. Conversely, the states near the Fermi energy are predominantly provided by the phosphorene substrate, leading to a decoupling of the magnetic and conductive charges. For the Mn atomic chain exhibiting the ferromagnetic state, a similar analysis is presented in Figs. 3(f), 3(g), and 3(i). We observe that the net spin charge also concentrates near the Mn atoms, as depicted in Fig. 3(f), with a charge isosurface set at $0.025e/\text{bohr}^3$. The band and DOS results exhibit a separation of the spin-up and spin-down charges, which respectively generate indirect band gaps of 0.70 and 0.23 eV. This asymmetric energy band structure can be shifted to intersect with its Fermi level by applying an external biasing or doping with donor or acceptor impurities, thereby forming a conductor whose conductivity is contributed solely by the spin-down electrons, indicating its potential as a modulated 1D spin current system [111–113].

Beyond the rich magnetic properties displayed by TM atomic chains, we have discovered multiple CDW configurations in the 1D Al atomic chains, attributable to structural distortion. Initially, we construct the unit cell, as shown by the black box in Fig. 4(a), with a single Al atom adsorbed. Upon sufficient relaxation, the Al atoms are uniformly spaced at a distance of 5.59 Å, a result of the periodic boundary constraint. Figure 4(b) illustrates the projected band structure and the DOS of this unit cell, with the k path referenced from the Brillouin zone in Fig. 2(b). Given that the Al atomic chain does not possess a net magnetic moment, the spin-up and spin-down charges are evenly distributed, resulting in a symmetric DOS. The system is classified as metallic, as the band intersects the Fermi energy, and the conducting charge near the Fermi level is primarily contributed by the Al element.

As established in Peierls theory, a 1D equally spaced metallic chain may undergo a metal-insulator (semiconductor) phase transition [114]. This transition is driven by structural distortion of the lattice, which reduces the total energy by splitting the band at the Fermi surface. Consequently, we double the size of the cell and perform a relaxation calculation at 0 K, with the final structure shown in Fig. 4(c). The Al atoms exhibit axial dimerization along the chain, where the distances between adjacent adatoms are alternately 5.37 Å and 5.84 Å, doubling the original lattice period, and the corresponding electronic properties are presented in Fig. 4(d). The energy of the distorted structure in Fig. 4(c), averaged per Al atom, is 36.7 meV lower than that in Fig. 4(a), and it validates that the system transitions from a conductor to an insulator, a CDW transformation primarily attributed to the Peierls mechanism. In fact, lattice distortions can give rise to multiple CDW states, since the total energy of the system during lattice distortion is

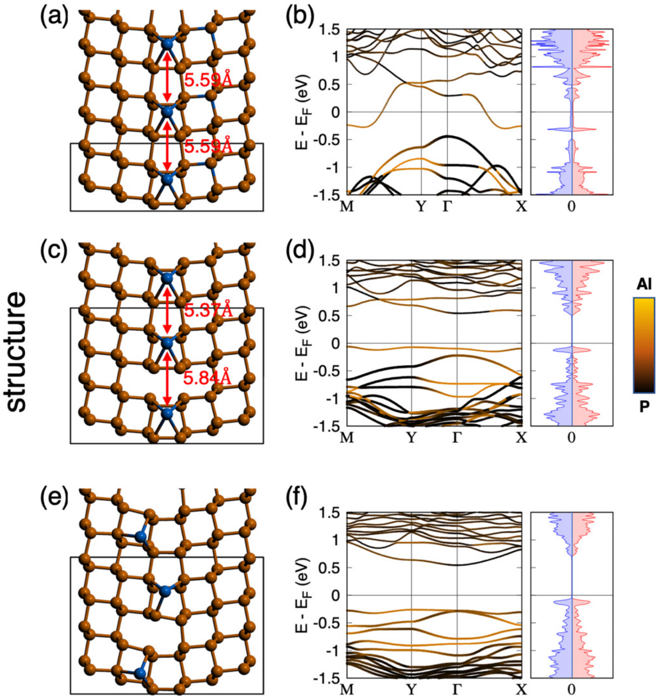

FIG. 4. The left-hand column respectively shows (a) the structures of the uniform Al chain, (c) the axial dimerized CDW configuration, and (e) the shear deformed CDW configuration. The unit cells used for calculations are denoted by black boxes, and the blue atoms represent Al adatoms. The distances between adjacent Al atoms have been measured and indicated in the graph. Correspondingly, the right-hand column [(b), (d), and (f)] displays the calculated projected bands and density of states (DOS) that correlate with the structural configurations of the left-hand figures.

affected by two antagonistic effects: the energy increase due to overcoming the elastic potential, and the energy decrease due to band splitting. To gain a deeper insight, we extend our exploration to other possible CDW configurations in Al atomic chains. As enlightened by discussions of Fig. 2(a), the adsorption energies of Al adatoms at sites A, B, and C are closely matched, facilitating the perpendicular slippage of the Al atom out of the TGB. We construct and identify the one indicated in Fig. 4(e) as the most stable CDW configuration. Here, the energy, averaged over each Al atom, is 162.8 meV lower than that in Fig. 4(a). The electronic information of the shear CDW state is displayed in Fig. 4(f), further corroborating the Peierls-type transition theory. In the Al atomic chain system, we have identified both axial and shear CDW transition modes, and similar phenomena are also observed in the iodine atomic chain encapsulated in a carbon nanotube [115].

Although various atomic chains are constructed utilizing the TGB template, it is of crucial importance to ascertain their stability at room temperature to facilitate subsequent research and applications. Prior researches have indicated that atomic arrangements and velocity distributions derived from AIMD simulations can be used for calculating phonon spectra at finite temperatures [116]. Moreover, it has been reported that the presence of imaginary-frequency modes in materials at 0 K does not necessarily exist at finite temperatures due to anharmonic effects [117]. Therefore, we employ AIMD calculations to verify the dynamical stability by observing the associated evolution of the atoms and structures. The following discussions mainly focus on the stability of atomic motion trajectories and magnetic moments, while the relevant results on the system temperatures and total energies are provided in the Supplemental Material as Figs. S7 and S8 [104]. For atomic chains coupled with the twinned phosphorene template, we perform 5000-step AIMD simulations, maintaining the basic parameters consistent with those in the 300 K tensile calculation. Besides, we incorporate spin polarization effects in consideration of the presence of metal adatoms, and apply the GGA + U method for the TM chains (V and Mn). The chosen supercell encompasses two metal adatoms, sufficient to characterize the magnetic orders and the CDW configurations. To minimize the interaction between adjacent chains, we double the width of the supercell. Finally, we assess the structural and magnetic stabilities by evaluating the fluctuations in atoms' spatial positions and the total magnetic moments over time, respectively.

We commence our investigation with the V and Mn atomic chain systems. The motion of each atom is visualized by plotting its trajectory from both top and side views, as displayed in Figs. 5(a) and 5(b), with the top and side views presented on the left and right, respectively. Given the strong binding of these two elements within the TGB channel, the trajectories of the atomic chains remain highly localized near their initial positions throughout the evolution process. Both systems remain stable, with no evidence of structural transition or breakdown. It is noteworthy that the trajectory diffusions of the V adatoms are less pronounced than those of Mn. This observation matches the adsorption energy calculation results, suggesting that V atoms ($E_{\mathrm{ad}} = -4.24$ eV) are more strongly trapped than the Mn atoms ($E_{\mathrm{ad}} = -2.66$ eV). In Fig. 5(c), the trajectory of the Al atomic chain indicates that one of the Al atoms slides outside the TGB, eventually settling in the adjacent locally stable potential well. At 0 K, it has been predicted that shear deformation would most significantly reduce the total energy. The room-temperature AIMD results corroborate this prediction, indicating that the Al chain is likely to transition from the axial to the shear distorted CDW state.

We proceed with an analysis of the magnetic stabilities for the V and Mn chains. As per the Mermin-Wagner theory [118], magnetic order is prohibited in isotropic 1D or 2D systems. Consequently, numerous studies have focused on identifying anisotropic low-dimensional structures that overcome this limitation and show magnetic orders at finite temperature, as reported in the Fe and Pt 1D spin chain systems [34,119], or in the $\mathrm{CrI_3}$ and $\mathrm{Cr_2Ge_2Te_6}$ 2D systems [120–122]. In light of this, we have performed computations at 0 K to determine the magnetic anisotropic energies (MAEs) of V and Mn atomic chains, which are 243 and 73 μeV/atom, respectively; therefore, it is anticipated that both systems will preserve their magnetic orders at low temperature. In addition, the magnetization easy axis for the V system lies along the direction of the atomic chain (in plane), while for the Mn system, it is perpendicular to the chain (out of plane). We then monitor the time-dependent behaviors of the magnetic moments at 300 K by AIMD simulations. As can be seen from Fig. 5(d), Mn and V systems separately exhibit a persistent total magnetic moment of approximately 10 μ_B (5 μ_B/atom)

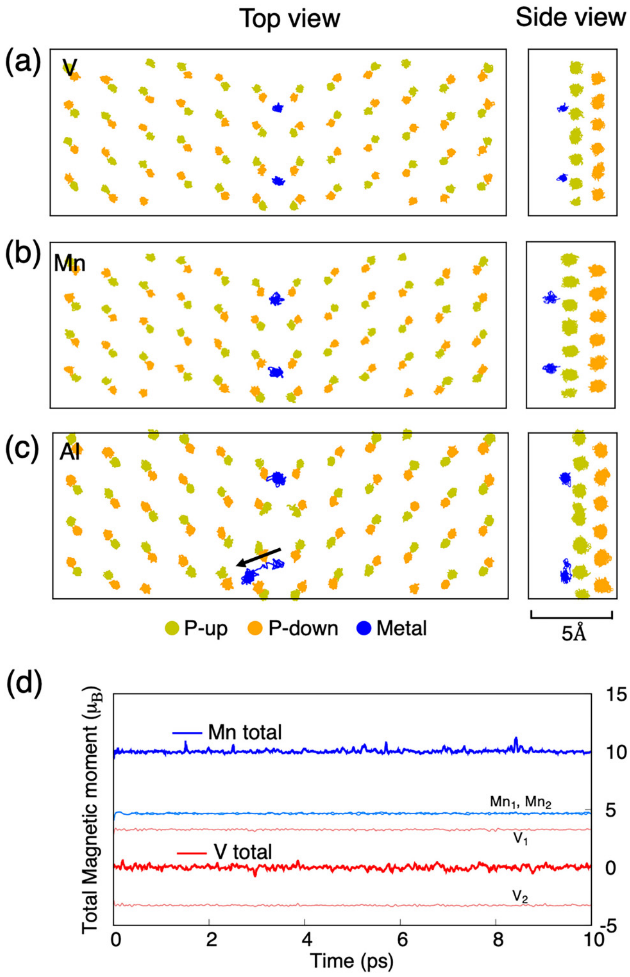

FIG. 5. [(a)-(c)] The top and side views of the atom trajectories from the AIMD simulations. The phosphorene atoms from the upper and lower layers are represented by green and orange tracks, respectively, while the adsorbed metal atoms are indicated by blue tracks. Simulation results for (a) V, (b) Mn, and (c) Al. (d) The time-dependent evolutions of the total magnetic moments for both V and Mn systems, as well as the time-dependent variations in the individual magnetic moments of transition metal atoms within each system.

and 0 μ_B, all exhibiting only slight fluctuations, indicating the TM adatoms can maintain their magnetic moments at room temperature. It should be emphasized that our focus in this work is more on the proposal of introducing the template for the preparation of atomic chains. In addition to the TM elements discussed in this paper, there are more elements with strong magnetic anisotropy, such as the $4f$ TM elements [123,124]. We will further investigate the atomic chains composed of these TM atoms on twinned phosphorene in future work, and hopefully compute the corresponding magnetic order phase transition temperatures using Monte Carlo simulations.

D. The manipulation of the TGB template and the construction of atomic rings

The twinned phosphorene template has been employed to construct a unique set of 1D stable atomic chains possessing distinctive properties. Here we will envision scenarios where the coupled system of twinned phosphorene and monatomic chains can be further manipulated and exploited. Research has revealed that spin chains are profoundly impacted by metal substrates due to the enhanced coupling effects, while they can enduringly maintain the intrinsic characteristics on semiconductive substrates. Hence we can affix the transferable phosphorene film onto a metal surface, where the spin chains exposed to the environment can retain their inherent properties due to the semiconductor nature of the phosphorene interlayer, and the metal substrate serves as a favorable conducting basis for precise measurements using STM probes. Moreover, the interaction between spin chains and superconducting materials may lead to the formation of 1D topological superconductors and the emergence of Majorana bound states. This advanced phenomenon can be achieved by directly attaching the atomic chain to a superconductor's surface. Beyond the direct transfer of the atomic chain system, we can construct a variety of 1D and zero-dimensional (0D) nanoarchitectures by manipulating the chains, and the corresponding possible configurations are illustrated in Fig. 6. These nanoarchitectures exhibit immense potential for the creation of a myriad of innovative low-dimensional structures for applications in the recently emerging curvilinear nanomagnetism.

As a showcase to demonstrate how the curvature of atomic chains can effectively change their physical properties, we consider hypothetical transition metal rings on the surfaces of twinned phosphorene nanotubes, as shown in Fig. 6(d). Given the robust stability and high localization of the V and Mn atomic chains on the TGB, here we directly scroll the V and Mn chains to create corresponding ring structures, as presented in Figs. 7(c)–7(f). In the system that encompasses the twinned phosphorene nanotube and the atomic ring, the diameter (or curvature) of the nanotube plays a significant role in affecting the stability. A smaller diameter could destabilize the system due to increased bending tension, while a larger diameter could potentially weaken the 0D physical characteristics of the quantum ring, as well as greatly increase the computation workload. Taking these factors into account, we investigate the six-ring and eight-ring structures, where the two types of structures comprise six and eight adatoms, and are associated with outer diameters of 14.0 and 17.4 Å, respectively.

Figure 7(c) illustrates the constructed V six-ring structure encircling the TGB of the nanotube. The left-hand graph presents a frontal view of the system, with the TGB emphasized by the blue shading. The six adatoms are coplanarly arranged, thus forming a precise ring structure. The top view of the portion highlighted in blue is displayed in the middle graph of Fig. 7(c), illustrating that the atomic ring is primarily situated on the surface of the nanotube, albeit with some embedment into the vacancies. The distances between adjacent adatoms are provided in the right-hand graph of Fig. 7(c), denoting that the V atoms are uniformly distributed with an interatomic distance of approximately 6.78 Å. To ascertain the preferential magnetic configuration of the system, we calculate the energy difference between the ferromagnetic and antiferromagnetic states ($\Delta E = E_{\text{ferro}} - E_{\text{antiferro}}$). Upon averaging over each V atom, the value of ΔE is found to be 6.8 meV/atom. Although the ring system favorably adopts an

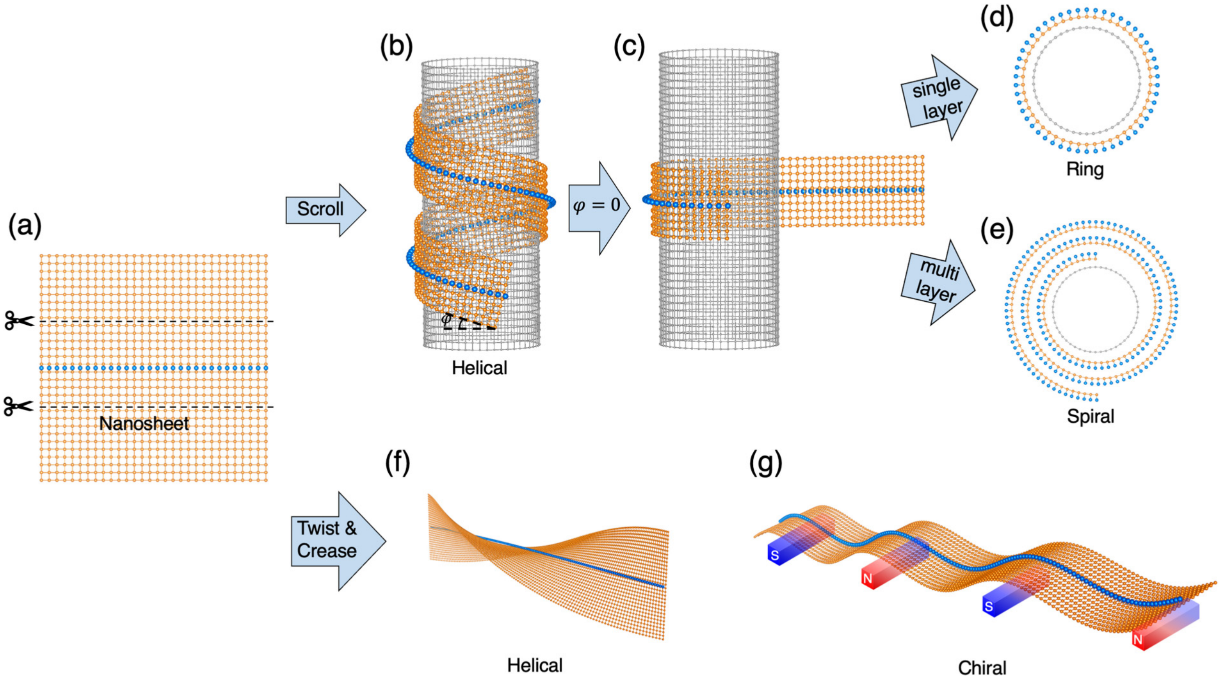

FIG. 6. The various approaches for manipulating the 1D atomic chain. (a) A 1D chain on a nanosheet can be fabricated by severing the monolayer twinned phosphorene along the delineated dotted line. (b) An equidistant helical chain can be configured by scrolling the nanosheet around a nanotube, with ϕ denoting the angle between the curling direction and the horizontal plane. [(c)–(e)] At $\phi = 0$, (d) an atomic ring or (e) an evolvent-shaped spiral chain can be constructed by circularly scrolling. (f) Another form of a helical spin chain can be constructed by twisting the two opposing ends of the nanosheet. (g) The chiral spin chain can be produced by inducing a crease into the nanosheet surface, featuring modifiable spin behaviors by employing an external magnetic field.

antiferromagnetic state, analogous to the 1D V atomic chain, the relatively small energy difference does not robustly guarantee magnetic stability at room temperature. We also apply this computational method to the V eight-ring system and present the findings in Fig. 7(d). For this system, ΔE increases to 20.8 meV/atom, and the enlarged value significantly bolsters the stability of the antiferromagnetic state. Examination of the middle graph in Fig. 7(d) manifests that the coplanar positioning of the V atoms persists in this system. However, adjacent atoms are seen to physically aggregate into pairs, resulting in new interatomic distances of 5.55 and 7.44 Å, as indicated in the right-hand graph of Fig. 7(d). To discern whether the observed dimerization arises from the deformation of the substrate, we execute relaxed calculations for the pure phosphorene tube devoid of adatoms, and the resulting six-tube and eight-tube structures are depicted in Figs. 7(a) and 7(b), respectively. Interestingly, the distances between adjacent vacancies are identical for both six- and eight-tube structures, thus ruling out the possibility of substrate-induced dimerization in the atomic chain. A more plausible explanation for the observed dimerization invokes a Jahn-Teller-effect-dominated structural distortion. This effect aids in expunging degeneracy and breaking symmetry, in turn augmenting system stability, and a similar phenomenon was also observed in the carbon rings [125].

In Figs. 7(e) and 7(f), we extend our analysis to the atomic rings formed by the ferromagnetic Mn atomic chain. The Mn six-ring structure, shown in Fig. 7(e), exhibits a coplanar and equally spaced configuration, favoring a ferromagnetic state characterized by a ΔE value of -8.2 meV/atom and a total magnetic moment of 30 μ_B. Moreover, the Mn eight-ring structure displayed in Fig. 7(f) presents even more evident structural dimerization, leading to an enhanced ferromagnetic state with a ΔE of -25.5 meV/atom and a total magnetic moment of 32 μ_B. In our examination of these atomic rings, we observed a tendency for adjacent atoms to dimerize as the ring diameter increases, thereby enhancing both the mechanical and magnetic stabilities of the structures. A probable justification for this behavior is that a smaller ring diameter gives rise to a considerable magnitude of tension within the nanotube, and thus the energy reduction facilitated by the Jahn-Teller-induced structural distortion does not suffice to counterbalance the accompanying increase in elastic potential energy. However, when the diameter of the ring enlarges, the nanotube relaxes, enabling the occurrence of structural distortion dominated by the Jahn-Teller effect. Overall, our proposed atomic ring systems are expected to exhibit stable ferromagnetic and antiferromagnetic states at low temperature, and the detailed electronic information pertaining to these systems can be found in the Supplemental Material (see Fig. S9) [104]. However, our work has focused solely on atomic rings with an even number of atoms. The consideration of odd-numbered atomic rings comprises more challenges, where periodic dimerization becomes untenable and antiferromagnetic V rings may therefore exhibit more complicated spin frustration phenomenon [126–128]. Unfortunately, deciphering the mechanisms behind this spin frustration cannot be accomplished directly via density functional theory methods and thereby necessitates further exploration through alternative research methodologies.

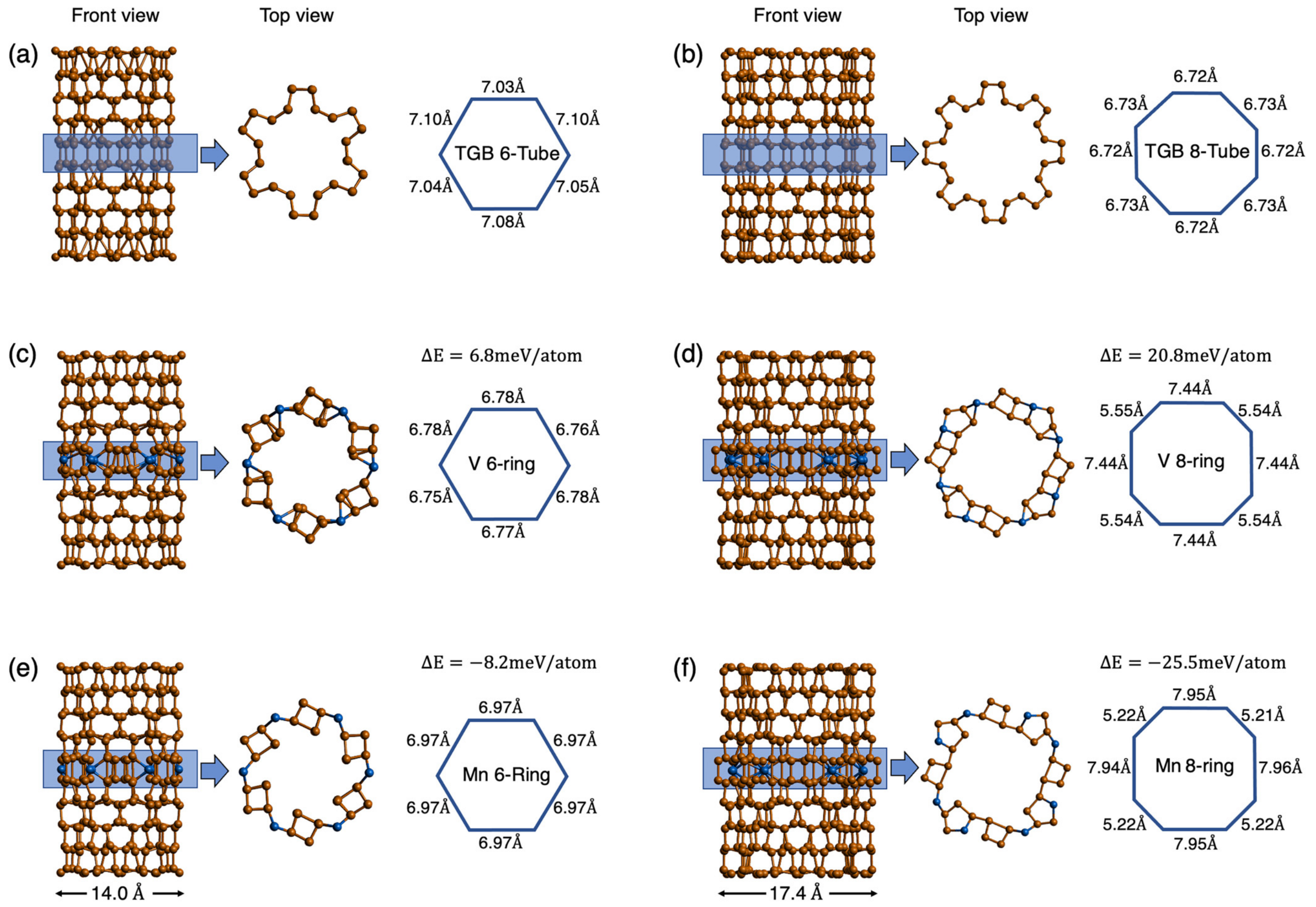

FIG. 7. (a) A schematic diagram of a pure phosphorene nanotube with six vacancies on the TGB surface, labeled as "6-Tube." The left-hand graph provides a front view where the TGB portion is denoted by blue shading, with its top perspective shown in the middle graph. On the right, a hexagonal representation details the distances between adjacent vacancies. A similar diagram is illustrated in (b) for the pure phosphorene eight-tube structure. (c) The coupled system of the phosphorene tube and a V atomic ring comprising six adatoms, designated as "V 6-ring." Here, the blue shading recognizes the TGB associated with the V atomic ring. The hexagon in the right-hand diagram presents the distances between the adjacent adatoms in the ring, with the value of energy difference between the two contrasting magnetic states ($\Delta E = E_{\mathrm{ferro}} - E_{\mathrm{antiferro}}$) computed. Corresponding analytical results are demonstrated for the (d) V eight-ring, (e) Mn six-ring, and (f) Mn eight-ring models.

IV. CONCLUSION

We propose the twinning-induced transition mechanism in phosphorene under in-plane stretching at room temperature—a different evolution from the ferroelastic phase transition at 0 K. Under such conditions, phosphorene exhibits a continuously tunable direct band gap with reducing anisotropic transport features, while still maintaining an exceptional elasticity of over 40%. In particular, the stretch-induced twinned phosphorene has been confirmed to support the construction of long-range-ordered, self-assembled one-dimensional atomic chains due to the presence of twinning grain boundaries, which feature one-dimensionally arranged channels adept at effectively capturing and localizing isolated atoms. A series of atomic chains has been thoroughly investigated, among which we discover that V and Mn atomic chains exhibit ferromagnetic and antiferromagnetic orders, respectively, while Al chains demonstrate CDWs in varying configurations as a consequence of a Peierls transition. More importantly, the coupled systems of twinned phosphorene and atomic chains may exhibit superior transferability and flexibility, showing potential in fabricating diverse curvilinear complex structures. An intriguing example from our work is the construction and analysis of even-numbered atomic ring systems, where the V and Mn rings demonstrate ferromagnetic and antiferromagnetic configurations, respectively, and both exhibit structural dimerized distortion dominated by the Jahn-Teller effects. In general, our work advances the comprehension of phosphorene's intrinsic mechanical and electronic properties at room temperature. The twinning structures emanating from our research significantly broaden the application of phosphorene as a functionalized nanoelectronic material, highlighting its potential in constructing linear and curvilinear low-dimensional nanostructures. Furthermore, this work paves new pathways for research of phosphorene along with its numerous analogs, and establishes fresh methodologies for the assembly of low-dimensional nanoarchitectures. This could have a profound impact on the exploration of low-dimensional quantum and topological phenomena, as well as on the development of miniaturized device platforms.

ACKNOWLEDGMENTS

This work was supported by the National Natural Science Foundation of China (Grant No. 11974237) and the Ministry of Science and Technology of the People's Republic of China (Grant No. 2016YFA0300500). The computations in this paper were run on the π 2.0 cluster supported by the Center for High Performance Computing at Shanghai Jiao Tong University.

---

[1] A. I. Yanson, G. R. Bollinger, H. E. van den Brom, N. Agraït, and J. M. van Ruitenbeek, Formation and manipulation of a metallic wire of single gold atoms, Nature (London) **395**, 783 (1998).

[2] E. H. Do and H. W. Yeom, Electron quantization in broken atomic wires, Phys. Rev. Lett. **115**, 266803 (2015).

[3] J. Zhang, K. Ishizuka, M. Tomitori, T. Arai, K. Hongo, R. Maezono, E. Tosatti, and Y. Oshima, Peculiar atomic bond nature in platinum monatomic chains, Nano Lett. **21**, 3922 (2021).

[4] O. Chiatti, J. T. Nicholls, Y. Y. Proskuryakov, N. Lumpkin, I. Farrer, and D. A. Ritchie, Quantum thermal conductance of electrons in a one-dimensional wire, Phys. Rev. Lett. **97**, 056601 (2006).

[5] L. Cui, W. Jeong, S. Hur, M. Matt, J. C. Klöckner, F. Pauly, P. Nielaba, J. C. Cuevas, E. Meyhofer, and P. Reddy, Quantized thermal transport in single-atom junctions, Science **355**, 1192 (2017).

[6] N. Papior, S. Leitherer, and M. Brandbyge, Simple approach to current-induced bond weakening in ballistic conductors, Phys. Rev. B **106**, 155401 (2022).

[7] Q. Wang, R. Liu, D. Xiang, M. Sun, Z. Zhao, L. Sun, T. Mei, P. Wu, H. Liu, X. Guo, Z.-L. Li, and T. Lee, Single-atom switches and single-atom gaps using stretched metal nanowires, ACS Nano **10**, 9695 (2016).

[8] N. Nilius, T. M. Wallis, and W. Ho, Development of one-dimensional band structure in artificial gold chains, Science **297**, 1853 (2002).

[9] G. V. Nazin, X. H. Qiu, and W. Ho, Atomic engineering of photon emission with a scanning tunneling microscope, Phys. Rev. Lett. **90**, 216110 (2003).

[10] T. Nagao, S. Yaginuma, T. Inaoka, and T. Sakurai, One-dimensional plasmon in an atomic-scale metal wire, Phys. Rev. Lett. **97**, 116802 (2006).

[11] J. Yan, Z. Yuan, and S. Gao, End and central plasmon resonances in linear atomic chains, Phys. Rev. Lett. **98**, 216602 (2007).

[12] F. Hötzel, K. Seino, C. Huck, O. Skibbe, F. Bechstedt, and A. Pucci, Metallic properties of the Si(111) - 5 × 2 - Au surface from infrared plasmon polaritons and ab initio theory, Nano Lett. **15**, 4155 (2015).

[13] T. Lichtenstein, Z. Mamiyev, C. Braun, S. Sanna, W. G. Schmidt, C. Tegenkamp, and H. Pfnür, Probing quasi-one-dimensional band structures by plasmon spectroscopy, Phys. Rev. B **97**, 165421 (2018).

[14] T. Yasuike, K. Nobusada, and M. Hayashi, Collectivity of plasmonic excitations in small sodium clusters with ring and linear structures, Phys. Rev. A **83**, 013201 (2011).

[15] N. Nayyar, V. Turkowski, and T. S. Rahman, Optical generation of collective plasmon modes in small gold chains induced by doping transition-metal impurities, Phys. Rev. Lett. **109**, 157404 (2012).

[16] K. M. Conley, N. Nayyar, T. P. Rossi, M. Kuisma, V. Turkowski, M. J. Puska, and T. S. Rahman, Plasmon excitations in mixed metallic nanoarrays, ACS Nano **13**, 5344 (2019).

[17] A. Weiße and H. Fehske, Peierls instability and optical response in the one-dimensional half-filled Holstein model of spinless fermions, Phys. Rev. B **58**, 13526 (1998).

[18] R. T. Clay and R. P. Hardikar, Intermediate phase of the one dimensional half-filled Hubbard-Holstein model, Phys. Rev. Lett. **95**, 096401 (2005).

[19] A. Abdelwahab and E. Jeckelmann, Luttinger liquid and charge density wave phases in a spinless fermion wire on a semiconducting substrate, Phys. Rev. B **98**, 235138 (2018).

[20] Y. Ohtsubo, J.-i. Kishi, K. Hagiwara, P. Le Fèvre, F. Bertran, A. Taleb-Ibrahimi, H. Yamane, S.-i. Ideta, M. Matsunami, K. Tanaka, and S.-i. Kimura, Surface Tomonaga-Luttinger-Liquid state on Bi/InSb(001), Phys. Rev. Lett. **115**, 256404 (2015).

[21] Y. Ohtsubo, J.-i. Kishi, K. Hagiwara, P. Le Fèvre, F. Bertran, A. Taleb-Ibrahimi, and S.-i. Kimura, Possible spin-charge separation of the Tomonaga-Luttinger liquid on Bi/InSb(001), J. Electron Spectrosc. Relat. Phenom. **220**, 37 (2017).

[22] R. Senaratne, D. Cavazos-Cavazos, S. Wang, F. He, Y.-T. Chang, A. Kafle, H. Pu, X.-W. Guan, and R. G. Hulet, Spin-charge separation in a 1D Fermi gas with tunable interactions, Science **376**, 1305 (2022).

[23] S. Cheon, T.-H. Kim, S.-H. Lee, and H. W. Yeom, Chiral solitons in a coupled double Peierls chain, Science **350**, 182 (2015).

[24] T.-H. Kim, S. Cheon, and H. W. Yeom, Switching chiral solitons for algebraic operation of topological quaternary digits, Nat. Phys. **13**, 444 (2017).

[25] G. Lee, H. Shim, J.-M. Hyun, and H. Kim, Intertwined solitons and impurities in a quasi-one-dimensional charge-density-wave system: In/Si(111), Phys. Rev. Lett. **122**, 016102 (2019).

[26] D.-J. Choi, N. Lorente, J. Wiebe, K. von Bergmann, A. F. Otte, and A. J. Heinrich, Colloquium: Atomic spin chains on surfaces, Rev. Mod. Phys. **91**, 041001 (2019).

[27] S. Nadj-Perge, I. K. Drozdov, J. Li, H. Chen, S. Jeon, J. Seo, A. H. MacDonald, B. A. Bernevig, and A. Yazdani, Observation of Majorana fermions in ferromagnetic atomic chains on a superconductor, Science **346**, 602 (2014).

[28] S. Jeon, Y. Xie, J. Li, Z. Wang, B. A. Bernevig, and A. Yazdani, Distinguishing a Majorana zero mode using spin-resolved measurements, Science **358**, 772 (2017).

[29] L. Schneider, P. Beck, J. Neuhaus-Steinmetz, L. Rózsa, T. Posske, J. Wiebe, and R. Wiesendanger, Precursors of Majorana modes and their length-dependent energy oscillations probed at both ends of atomic Shiba chains, Nat. Nanotechnol. **17**, 384 (2022).

[30] A. A. Khajetoorians, J. Wiebe, B. Chilian, and R. Wiesendanger, Realizing all-spin-based logic operations atom by atom, Science **332**, 1062 (2011).

[31] J. Klinovaja, P. Stano, A. Yazdani, and D. Loss, Topological superconductivity and Majorana fermions in RKKY systems, Phys. Rev. Lett. **111**, 186805 (2013).

[32] M. Menzel, Y. Mokrousov, R. Wieser, J. E. Bickel, E. Vedmedenko, S. Blügel, S. Heinze, K. von Bergmann, A. Kubetzka, and R. Wiesendanger, Information transfer by vector spin chirality in finite magnetic chains, Phys. Rev. Lett. **108**, 197204 (2012).

[33] M. Steinbrecher, R. Rausch, K. T. That, J. Hermenau, A. A. Khajetoorians, M. Potthoff, R. Wiesendanger, and J. Wiebe, Non-collinear spin states in bottom-up fabricated atomic chains, Nat. Commun. **9**, 2853 (2018).

[34] C. F. Hirjibehedin, C. P. Lutz, and A. J. Heinrich, Spin coupling in engineered atomic structures, Science **312**, 1021 (2006).

[35] S. Loth, S. Baumann, C. P. Lutz, D. M. Eigler, and A. J. Heinrich, Bistability in atomic-scale antiferromagnets, Science **335**, 196 (2012).

[36] J. Aulbach, S. C. Erwin, R. Claessen, and J. Schäfer, Spin chains and electron transfer at stepped silicon surfaces, Nano Lett. **16**, 2698 (2016).

[37] Z. Mamiyev, C. Fink, K. Holtgrewe, H. Pfnür, and S. Sanna, Enforced long-range order in 1D wires by coupling to higher dimensions, Phys. Rev. Lett. **126**, 106101 (2021).

[38] L. Guan, K. Suenaga, S. Okubo, T. Okazaki, and S. Iijima, Metallic wires of lanthanum atoms inside carbon nanotubes, J. Am. Chem. Soc. **130**, 2162 (2008).

[39] T. Fujimori, A. Morelos-Gómez, Z. Zhu, H. Muramatsu, R. Futamura, K. Urita, M. Terrones, T. Hayashi, M. Endo, S. Young Hong, Y. Chul Choi, D. Tománek, and K. Kaneko, Conducting linear chains of sulphur inside carbon nanotubes, Nat. Commun. **4**, 2162 (2013).

[40] R. Senga, H.-P. Komsa, Z. Liu, K. Hirose-Takai, A. V. Krasheninnikov, and K. Suenaga, Atomic structure and dynamic behaviour of truly one-dimensional ionic chains inside carbon nanotubes, Nat. Mater. **13**, 1050 (2014).

[41] H. Liu, A. T. Neal, Z. Zhu, Z. Luo, X. Xu, D. Tománek, and P. D. Ye, Phosphorene: An unexplored 2D semiconductor with a high hole mobility, ACS Nano **8**, 4033 (2014).

[42] V. Tran, R. Soklaski, Y. Liang, and L. Yang, Layer-controlled band gap and anisotropic excitons in few-layer black phosphorus, Phys. Rev. B **89**, 235319 (2014).

[43] K. S. Novoselov, A. K. Geim, S. V. Morozov, D. Jiang, M. I. Katsnelson, I. V. Grigorieva, S. V. Dubonos, and A. A. Firsov, Two-dimensional gas of massless Dirac fermions in graphene, Nature (London) **438**, 197 (2005).

[44] Q. H. Wang, K. Kalantar-Zadeh, A. Kis, J. N. Coleman, and M. S. Strano, Electronics and optoelectronics of two-dimensional transition metal dichalcogenides, Nat. Nanotechnol. **7**, 699 (2012).

[45] F. Xia, H. Wang, D. Xiao, M. Dubey, and A. Ramasubramaniam, Two-dimensional material nanophotonics, Nat. Photon. **8**, 899 (2014).

[46] J. Qiao, X. Kong, Z.-X. Hu, F. Yang, and W. Ji, High-mobility transport anisotropy and linear dichroism in few-layer black phosphorus, Nat. Commun. **5**, 4475 (2014).

[47] A. Jain and A. J. H. McGaughey, Strongly anisotropic in-plane thermal transport in single-layer black phosphorene, Sci. Rep. **5**, 8501 (2015).

[48] M. Wu and X. C. Zeng, Intrinsic ferroelasticity and/or multiferroicity in two-dimensional phosphorene and phosphorene analogues, Nano Lett. **16**, 3236 (2016).

[49] R. Fei and L. Yang, Strain-engineering the anisotropic electrical conductance of few-layer black phosphorus, Nano Lett. **14**, 2884 (2014).

[50] D. Q. Khoa, M. Davoudiniya, B. D. Hoi, and M. Yarmohammadi, Strain engineering of optical activity in phosphorene, RSC Adv. **9**, 19006 (2019).

[51] A. Khandelwal, K. Mani, M. H. Karigerasi, and I. Lahiri, Phosphorene—the two-dimensional black phosphorous: Properties, synthesis and applications, Mater. Sci. Eng. B **221**, 17 (2017).

[52] S. S. P. Parkin, M. Hayashi, and L. Thomas, Magnetic domain-wall racetrack memory, Science **320**, 190 (2008).

[53] M.-A. Mawass, K. Richter, A. Bisig, R. M. Reeve, B. Krüger, M. Weigand, H. Stoll, A. Krone, F. Kronast, G. Schütz, and M. Kläui, Switching by domain-wall automotion in asymmetric ferromagnetic rings, Phys. Rev. Appl. **7**, 044009 (2017).

[54] S. Parkin and S.-H. Yang, Memory on the racetrack, Nat. Nanotechnol. **10**, 195 (2015).

[55] O. M. Volkov, A. Kákay, F. Kronast, I. Mönch, M.-A. Mawass, J. Fassbender, and D. Makarov, Experimental observation of exchange-driven chiral effects in curvilinear magnetism, Phys. Rev. Lett. **123**, 077201 (2019).

[56] C. Donnelly, A. Hierro-Rodríguez, C. Abert, K. Witte, L. Skoric, D. Sanz-Hernández, S. Finizio, F. Meng, S. McVitie, J. Raabe, D. Suess, R. Cowburn, and A. Fernández-Pacheco, Complex free-space magnetic field textures induced by three-dimensional magnetic nanostructures, Nat. Nanotechnol. **17**, 136 (2022).

[57] D. Sanz-Hernández, A. Hierro-Rodriguez, C. Donnelly, J. Pablo-Navarro, A. Sorrentino, E. Pereiro, C. Magén, S. McVitie, J. M. De Teresa, S. Ferrer, P. Fischer, and A. Fernández-Pacheco, Artificial double-helix for geometrical control of magnetic chirality, ACS Nano **14**, 8084 (2020).

[58] J. G. Gibbs, A. G. Mark, T.-C. Lee, S. Eslami, D. Schamel, and P. Fischer, Nanohelices by shadow growth, Nanoscale **6**, 9457 (2014).

[59] I. Mönch, D. Makarov, R. Koseva, L. Baraban, D. Karnaushenko, C. Kaiser, K.-F. Arndt, and O. G. Schmidt, Rolled-up magnetic sensor: Nanomembrane architecture for in-flow detection of magnetic objects, ACS Nano **5**, 7436 (2011).

[60] C. Becker, D. Karnaushenko, T. Kang, D. D. Karnaushenko, M. Faghih, A. Mirhajivarzaneh, and O. G. Schmidt, Self-assembly of highly sensitive 3D magnetic field vector angular encoders, Sci. Adv. **5**, eaay7459 (2019).

[61] D. Karnaushenko, D. D. Karnaushenko, D. Makarov, S. Baunack, R. Schäfer, and O. G. Schmidt, Self-assembled on-chip-integrated giant magneto-impedance sensorics, Adv. Mater. **27**, 6582 (2015).

[62] A. Chiesa, T. Guidi, S. Carretta, S. Ansbro, G. A. Timco, I. Vitorica-Yrezabal, E. Garlatti, G. Amoretti, R. E. P. Winpenny, and P. Santini, Magnetic exchange interactions in the molecular nanomagnet Mn_{12}, Phys. Rev. Lett. **119**, 217202 (2017).

[63] L. Thomas, F. R. Lionti, R. Ballou, D. Gatteschi, and B. Barbara, Macroscopic quantum tunnelling of magnetization in a single crystal of nanomagnets, Nature (London) **383**, 145 (1996).

[64] W. Wernsdorfer and R. Sessoli, Quantum phase interference and parity effects in magnetic molecular clusters, Science **284**, 133 (1999).

[65] M. N. Leuenberger and D. Loss, Quantum computing in molecular magnets, Nature (London) **410**, 789 (2001).

[66] L. Bogani and W. Wernsdorfer, Molecular spintronics using single-molecule magnets, Nat. Mater. **7**, 179 (2008).

[67] E. Moreno-Pineda and W. Wernsdorfer, Measuring molecular magnets for quantum technologies, Nat. Rev. Phys. **3**, 645 (2021).

[68] T. Jungwirth, X. Marti, P. Wadley, and J. Wunderlich, Antiferromagnetic spintronics, Nat. Nanotechnol. **11**, 231 (2016).

[69] K. L. Taft, C. D. Delfs, G. C. Papaefthymiou, S. Foner, D. Gatteschi, and S. J. Lippard, $[Fe(OMe)_2(O_2CCH2Cl)]_{10}$, a molecular ferric wheel, J. Am. Chem. Soc. **116**, 823 (1994).

[70] O. Waldmann, T. Guidi, S. Carretta, C. Mondelli, and A. L. Dearden, Elementary excitations in the cyclic molecular nanomagnet Cr_8, Phys. Rev. Lett. **91**, 237202 (2003).

[71] O. Waldmann, C. Dobe, S. T. Ochsenbein, H. U. Güdel, and I. Sheikin, Field-induced magnetoelastic instabilities in antiferromagnetic molecular wheels, Phys. Rev. Lett. **96**, 027206 (2006).

[72] V. Lante, I. Rousochatzakis, K. Penc, O. Waldmann, and F. Mila, Spin-Peierls instabilities of antiferromagnetic rings in a magnetic field, Phys. Rev. B **79**, 180412(R) (2009).

[73] Ch. Rüegg, N. Cavadini, A. Furrer, H.-U. Güdel, K. Krämer, H. Mutka, A. Wildes, K. Habicht, and P. Vorderwisch, Bose-Einstein condensation of the triplet states in the magnetic insulator $TlCuCl_3$, Nature (London) **423**, 62 (2003).

[74] S. Kimura, M. Matsumoto, and H. Tanaka, Electrical switching of the nonreciprocal directional microwave response in a triplon Bose-Einstein condensate, Phys. Rev. Lett. **124**, 217401 (2020).

[75] B. Lenz, B. Koteswararao, S. Biermann, P. Khuntia, M. Baenitz, and S. K. Panda, The $S = 1$ dimer system $K_2Ni(MoO_4)_2$: A candidate for magnon Bose-Einstein condensation, Phys. Rev. B **106**, L180408 (2022).

[76] T. G. Tziotzi, D. Gracia, S. J. Dalgarno, J. Schnack, M. Evangelisti, E. K. Brechin, and C. J. Milios, A $\{Gd_{12}Na_6\}$ molecular quadruple-wheel with a record magnetocaloric effect at low magnetic fields and temperatures, J. Am. Chem. Soc. **145**, 7743 (2023).

[77] J. W. Sharples, D. Collison, E. J. L. McInnes, J. Schnack, E. Palacios, and M. Evangelisti, Quantum signatures of a molecular nanomagnet in direct magnetocaloric measurements, Nat. Commun. **5**, 5321 (2014).

[78] F. Troiani, A. Ghirri, M. Affronte, S. Carretta, P. Santini, G. Amoretti, S. Piligkos, G. Timco, and R. E. P. Winpenny, Molecular engineering of antiferromagnetic rings for quantum computation, Phys. Rev. Lett. **94**, 207208 (2005).

[79] C. J. Wedge, G. A. Timco, E. T. Spielberg, R. E. George, F. Tuna, S. Rigby, E. J. L. McInnes, R. E. P. Winpenny, S. J. Blundell, and A. Ardavan, Chemical engineering of molecular qubits, Phys. Rev. Lett. **108**, 107204 (2012).

[80] J. Ferrando-Soria, E. Moreno Pineda, A. Chiesa, A. Fernandez, S. A. Magee, S. Carretta, P. Santini, I. J. Vitorica-Yrezabal, F. Tuna, G. A. Timco, E. J. McInnes, and R. E. Winpenny, A modular design of molecular qubits to implement universal quantum gates, Nat. Commun. **7**, 11377 (2016).

[81] S. J. Lockyer, A. Chiesa, G. A. Timco, E. J. L. McInnes, T. S. Bennett, I. J. Vitorica-Yrezebal, S. Carretta, and R. E. P. Winpenny, Targeting molecular quantum memory with embedded error correction, Chem. Sci. **12**, 9104 (2021).

[82] C. Kamal and M. Ezawa, Arsenene: Two-dimensional buckled and puckered honeycomb arsenic systems, Phys. Rev. B **91**, 085423 (2015).

[83] O. Ü. Aktürk, V. O. Özçelik, and S. Ciraci, Single-layer crystalline phases of antimony: Antimonenes, Phys. Rev. B **91**, 235446 (2015).

[84] H. A. Jahn and E. Teller, Stability of polyatomic molecules in degenerate electronic states. I. Orbital degeneracy, Proc. Math. Phys. Eng. Sci. **161**, 220 (1937).

[85] G. Kresse and J. Furthmüller, Efficient iterative schemes for *ab initio* total-energy calculations using a plane-wave basis set, Phys. Rev. B **54**, 11169 (1996).

[86] G. Kresse and D. Joubert, From ultrasoft pseudopotentials to the projector augmented-wave method, Phys. Rev. B **59**, 1758 (1999).

[87] J. P. Perdew, K. Burke, and M. Ernzerhof, Generalized gradient approximation made simple, Phys. Rev. Lett. **77**, 3865 (1996).

[88] H. J. Monkhorst and J. D. Pack, Special points for Brillouin-zone integrations, Phys. Rev. B **13**, 5188 (1976).

[89] S. Grimme, J. Antony, S. Ehrlich, and H. Krieg, A consistent and accurate *ab initio* parametrization of density functional dispersion correction (DFT-D) for the 94 elements H–Pu, J. Chem. Phys. **132**, 154104 (2010).

[90] G. Henkelman and H. Jónsson, Improved tangent estimate in the nudged elastic band method for finding minimum energy paths and saddle points, J. Chem. Phys. **113**, 9978 (2000).

[91] G. Henkelman, B. P. Uberuaga, and H. Jónsson, A climbing image nudged elastic band method for finding saddle points and minimum energy paths, J. Chem. Phys. **113**, 9901 (2000).

[92] Z. Pan, H. Sun, Y. Zhang, and C. Chen, Harder than diamond: Superior indentation strength of wurtzite BN and lonsdaleite, Phys. Rev. Lett. **102**, 055503 (2009).

[93] B. Li, H. Sun, and C. Chen, Extreme mechanics of probing the ultimate strength of nanotwinned diamond, Phys. Rev. Lett. **117**, 116103 (2016).

[94] M. Parrinello and A. Rahman, Crystal structure and pair potentials: A molecular-dynamics study, Phys. Rev. Lett. **45**, 1196 (1980).

[95] L. Wen, H. Wu, H. Sun, and C. Chen, Profound softening and shear-induced melting of diamond under extreme conditions: An *ab-initio* molecular dynamics study, Carbon **155**, 361 (2019).

[96] M. Yang and H. Sun, Early melting of tantalum carbide under anisotropic stresses: An *ab initio* molecular dynamics study, Phys. Rev. B **107**, 104101 (2023).

[97] M. Alen and D. Tildesley, *Computer Simulations of Liquids* (Oxford University Press, Oxford, UK, 1991).

[98] Q. Wei and X. Peng, Superior mechanical flexibility of phosphorene and few-layer black phosphorus, Appl. Phys. Lett. **104**, 251915 (2014).

[99] A. S. Rodin, A. Carvalho, and A. H. Castro Neto, Strain-induced gap modification in black phosphorus, Phys. Rev. Lett. **112**, 176801 (2014).

[100] F. Xia, H. Wang, and Y. Jia, Rediscovering black phosphorus as an anisotropic layered material for optoelectronics and electronics, Nat. Commun. **5**, 4458 (2014).

[101] T. Hu and J. Dong, Structural phase transitions of phosphorene induced by applied strains, Phys. Rev. B **92**, 064114 (2015).

[102] B. W. Li, Y. Wang, Y. Q. Xie, L. Zhu, and K. L. Yao, Strain controlled switching effects in phosphorene and GeS, Nanotechnology **28**, 435202 (2017).

[103] S. Zhang and H. Sun, Effects of temperature on strain engineering and transition-metal adatom magnetization in phosphorene: *Ab initio* molecular dynamics studies, Phys. Rev. B **103**, 155432 (2021).

[104] See Supplemental Material at http://link.aps.org/supplemental/10.1103/PhysRevB.109.104105 for more details,including the AIMD time steps for the gradual structural transitions at 300 K, the rationality analysis for the twinning transition mechanism, PDOS of pristine phosphorene and twinned phosphorene, the relative adsorption energy heat maps for other elements (V, Cr, Fe, and Al), the effect of supercell sizes on the adsorption energies of TM adatoms, the relation between AIMD simulation calculations and structural dynamical stability, and the DOS results of the nanotubes and atomic rings coupled systems.

[105] W. Jang, K. Kang, and A. Soon, Remarkably low-energy one-dimensional fault line defects in single-layered phosphorene, Nanoscale **7**, 19073 (2015).

[106] J. Guan, K. Li, N. Lu, and C. Yang, Unique low-energy line defects and lateral heterostructures in phosphorene, Phys. Scr. **98**, 015815 (2023).

[107] R. Zhang, X. Wu, and J. Yang, Blockage of ultrafast and directional diffusion of Li atoms on phosphorene with intrinsic defects, Nanoscale **8**, 4001 (2016).

[108] S. M. Atashzar, S. Javadian, H. Gharibi, and Z. Rezaei, Defective phosphorene as an anode material for high-performance Li-, Na-, and K-ion batteries: A first-principles study, Nanoscale **12**, 20364 (2020).

[109] P. Srivastava, K. P. S. S. Hembram, H. Mizuseki, K.-R. Lee, S. S. Han, and S. Kim, Tuning the electronic and magnetic properties of phosphorene by vacancies and adatoms, J. Phys. Chem. C **119**, 6530 (2015).

[110] M. Cococcioni and S. de Gironcoli, Linear response approach to the calculation of the effective interaction parameters in the LDA + U method, Phys. Rev. B **71**, 035105 (2005).

[111] Y. Guo, B. Wang, X. Zhang, S. Yuan, L. Ma, and J. Wang, Magnetic two-dimensional layered crystals meet with ferromagnetic semiconductors, InfoMat **2**, 639 (2020).

[112] I. Žutić and H. Dery, Taming spin currents, Nat. Mater. **10**, 647 (2011).

[113] S. Murakami, N. Nagaosa, and S.-C. Zhang, Dissipationless quantum spin current at room temperature, Science **301**, 1348 (2003).

[114] S. R. Peierls, *Quantum Theory of Solids* (Clarendon, Oxford, UK, 1963).

[115] H.-P. Komsa, R. Senga, K. Suenaga, and A. V. Krasheninnikov, Structural distortions and charge density waves in iodine chains encapsulated inside carbon nanotubes, Nano Lett. **17**, 3694 (2017).

[116] D.-B. Zhang, T. Sun, and R. M. Wentzcovitch, Phonon quasiparticles and anharmonic free energy in complex systems, Phys. Rev. Lett. **112**, 058501 (2014).

[117] T. Sun, D.-B. Zhang, and R. M. Wentzcovitch, Dynamic stabilization of cubic $CaSiO_3$ perovskite at high temperatures and pressures from *ab initio* molecular dynamics, Phys. Rev. B **89**, 094109 (2014).

[118] N. D. Mermin and H. Wagner, Absence of ferromagnetism or antiferromagnetism in one- or two-dimensional isotropic Heisenberg models, Phys. Rev. Lett. **17**, 1133 (1966).

[119] A. Spinelli, B. Bryant, F. Delgado, J. Fernández-Rossier, and A. F. Otte, Imaging of spin waves in atomically designed nanomagnets, Nat. Mater. **13**, 782 (2014).

[120] B. Huang, G. Clark, E. Navarro-Moratalla, D. R. Klein, R. Cheng, K. L. Seyler, D. Zhong, E. Schmidgall, M. A. McGuire, D. H. Cobden, W. Yao, D. Xiao, P. Jarillo-Herrero, and X. Xu, Layer-dependent ferromagnetism in a van der Waals crystal down to the monolayer limit, Nature (London) **546**, 270 (2017).

[121] S. Jiang, L. Li, Z. Wang, K. F. Mak, and J. Shan, Controlling magnetism in 2D CrI_3 by electrostatic doping, Nat. Nanotechnol. **13**, 549 (2018).

[122] C. Gong, L. Li, Z. Li, H. Ji, A. Stern, Y. Xia, T. Cao, W. Bao, C. Wang, Y. Wang, Z. Q. Qiu, R. J. Cava, S. G. Louie, J. Xia, and X. Zhang, Discovery of intrinsic ferromagnetism in two-dimensional van der Waals crystals, Nature (London) **546**, 265 (2017).

[123] C. Gao, A. Genoni, S. Gao, S. Jiang, A. Soncini, and J. Overgaard, Observation of the asphericity of $4f$-electron density and its relation to the magnetic anisotropy axis in single-molecule magnets, Nat. Chem. **12**, 213 (2020).

[124] S. Gómez-Coca, D. Aravena, R. Morales, and E. Ruiz, Large magnetic anisotropy in mononuclear metal complexes, Coord. Chem. Rev. **289–290**, 379 (2015).

[125] I. Hong, J. Ahn, H. Shin, H. Bae, H. Lee, A. Benali, and Y. Kwon, Competition between Hückel's rule and Jahn-Teller distortion in small carbon rings: A quantum Monte Carlo study, J. Phys. Chem. A **124**, 3636 (2020).

[126] V. Fritsch, J. Hemberger, N. Büttgen, E.-W. Scheidt, H.-A. Krug von Nidda, A. Loidl, and V. Tsurkan, Spin and orbital frustration in $MnSc_2S_4$ and $FeSc_2S_4$, Phys. Rev. Lett. **92**, 116401 (2004).

[127] R. Moessner and A. P. Ramirez, Geometrical frustration, Phys. Today **59**(2), 24 (2006).

[128] N. Hoshino, M. Nakano, H. Nojiri, W. Wernsdorfer, and H. Oshio, Templating odd numbered magnetic rings: Oxovanadium heptagons sandwiched by β-cyclodextrins, J. Am. Chem. Soc. **131**, 15100 (2009).